Spatial and temporal control of quantum dots for on-chip integration

by

Jieun Lee

A dissertation submitted in partial fulfillment
of the requirements for the degree of
Doctor of Philosophy
(Physics)
in the University of Michigan
2014

Doctoral committee:

Assistant Professor Vanessa Sih, Chair
Assistant Professor Xiaoming Mao
Professor Joanna M. Millunchick
Professor Georg A. Raithel
Professor Duncan G. Steel

Copyright © 2014

by

Jieun Lee

Acknowledgements

I would like to thank the many people who have helped me on the path towards this thesis.

First, I sincerely appreciate my thesis advisor, Vanessa Sih, for her wonderful guidance. Her support, patience and enthusiasm on research were great encouragements for me to pursue graduate studies.

I am also grateful for all current and former members of our group. In particular, I thank Ben Norman, Tim Saucer and Chris Trowbridge for their knowledge and efforts to introduce the lab equipments to me. Also, I would like to express many thanks to Marta Luengo-Kovac, Michael Macmahon and Brennan Pursley for making the lab an enjoyable place to conduct research. I wish the best of luck to the newest members of the group, Xinlin Song and Aneesh Venugopal.

Many thanks to collaborators who have contributed to my research. I am especially indebted to Andrew Martin from the Millunchick group who grew quantum dot samples for us which was the foundation of this thesis work. I also very much enjoyed conducting experiments with Sunyeol Jeon and Myungkoo Kang from the Goldman group.

I appreciate my committee members including Xiaoming Mao and Georg Raithel for their help to complete this thesis. In particular, I would like to thank Joanna Millunchick for her valuable advice and contributions to the quantum dot experiments. I am also thankful to Duncan Steel for fruitful discussions on interpreting our experiments and building a theoretical background.

Many people in the Lurie Nanofabrication Facility greatly helped me to make photonic crystals. I would like to thank Greg Allion, Robert Hower and Vishva Ray and other staff for sharing their knowledge and experience.

I am also grateful to professors Jeongsoo Kang, Yoon-Ho Kim and Byung Il Min who encouraged me to do summer undergraduate research participation and Master degree research at Pohang University of Science and Technology.

Finally, I wish to thank my family for their love and support during the journey of my PhD study.

Contents

List of Figures

List of Tables

List of Appendices

Abstract

Quantum dots are nanostructures that confine electrons in three spatial dimensions. Due to their discrete atom-like energy levels and localization from the environment, individual quantum dots have the potential to be used as solid-state qubits for quantum information processing. To enable such information processing in a scalable manner, it is necessary to integrate quantum dots on-chip to devices like photonic crystal cavities for building a hybrid interface of a light-matter coupled system. Motivated to develop an effective way to integrate quantum dots with photonic crystals, this thesis first investigates spatially controlled InAs quantum dots that are fabricated by focused-ion-beam milling and molecular-beam epitaxy. Here, multi-layers of InAs quantum dots on top of the site-controlled seed dots are fabricated and the linewidth of an individual dot as narrow as 160 μeV is measured, indicating an improved optical quality over single-layer quantum dot samples. In addition, a spatial map of the micro-photoluminescence of individual quantum dots is measured to verify the dot positions with diffraction-limited spatial resolution. Statistical analysis over 16 array sites shows that the seed dot positions have transferred to the upper layers with a finite spatial deviation due to the formation of mounds. In addition to an optical study of site-controlled quantum dots, the second part of this thesis investigates the temporal dynamics of self-assembled InAs quantum dots that are coupled to a photonic crystal cavity. By performing the luminescence intensity autocorrelation experiment, the Purcell enhanced emission from individual quantum dots resonant to a cavity mode is measured, demonstrating a temporal

control of quantum dots through coupling to an optical nanocavity. The measurement of exciton and biexciton transitions reveals distinct autocorrelation signals which originate from their different nonlinearities. Finally, a quantum optical simulation incorporating the interaction between the laser pulses, cavity mode and atomic two-level system is used to support the experimental exciton autocorrelation data.

Chapter 1

Introduction

Semiconductor quantum dots coupled to optical nanocavities are relevant to and require the understanding of several fields including quantum mechanics, condensed-matter physics, nanoscience and quantum optics. Quantum dots are artificial structures that can confine electrons within a small volume in a manner that is similar to how electrons are bound in atoms. Also, nanocavities can confine light similar to more conventional optical cavities, such as the Fabry-Perot interferometer, and can be fabricated with a size as small as a cubic optical wavelength. By coupling quantum dots to optical nanocavities, we are able to create a light-matter interaction interface resembling an atom-cavity coupled system on a miniaturized chip. Such coupling between quantum dots and nanocavities is expected to provide an interesting platform to study cavity quantum electrodynamics (QED). In this work, we explore methods to fabricate optimized quantum dots and examine their optical properties and study quantum dot-cavity interactions in relation to nonlinearities and emission dynamics.

1.1 Background

The ability to achieve light-matter interaction using solid-state nanostructures has provoked interests in realizing quantum information processing on a miniaturized chip [1]. In order to realize information processing, it is necessary to initialize, manipulate, transport and read-out information [2]. In earlier experiments, it has been found that quantum dots can generate single photons that can be used as qubits [3, 4]. Researchers demonstrated that spins of quantum dots can also work as qubits through optical initialization [5] and gate operations [6].

To enable information processing using quantum dots, we need to efficiently generate single photons, couple spatially separated quantum dots together and enhance the interaction between the dots and photons, which can be achieved by integrating dots in photonic crystals. Coupling quantum dots to photonic crystals has demonstrated the enhanced spontaneous emission rate of dots [7], giant optical nonlinearity using a few photons [8–11], coherent strong coupling [12, 13] and the possibility to entangle a dot with cavity photons [14]. Thus, cavity QED in solid-state is promising for creating an efficient hybrid interface between light and matter to enable photonic networking.

However, quantum dots are solid-state materials which require techniques to regulate them as qubits. For example, epitaxial quantum dots are typically grown with random locations which is detrimental for coupling to photonic crystals. Therefore, there has been a lot of efforts to deterministically couple quantum dots to photonic cavities by locating a dot and fabricating a cavity around it [13] or site-controlling the dots at the fabrication level [15–25]. In addition, to enable photon processing using quantum dots and cavity, it is necessary to understand their nonlinearity and develop tools to quantify the coupling dynamics [8]. Nonlinearity in the strong coupling regime has shown that the system can be used as an ultrafast photon switch [10] while fewer studies have been reported about nonlinearity in the

Purcell regime.

1.2 Results

My work focuses on investigating quantum dots grown by a site-controlled method and nonlinear dynamics observed when quantum dots are coupled to a photonic crystal cavity in the Purcell regime.

First, I carried out photoluminescence imaging of site-controlled single quantum dots with diffraction-limited optical resolution to determine their optical quality and fidelity for practical applications. The site-control of the dots was achieved by focused-ion-beam patterning in collaboration with the group of Prof. Joanna Millunchick in the Department of Materials Science and Engineering. The optical quality was improved by vertically stacking quantum dots on top of the seed dots, demonstrating single quantum dot exciton line width of 160 μeV using micro-photoluminescence. In addition, we spatially mapped the photoluminescence of individual dots in the sample using scanning confocal microscopy over 10 $\times$ 10 μm^2 for a statistical analysis.

Second, I designed and fabricated photonic crystal cavities with embedded quantum dots and investigated the nonlinear emission dynamics of quantum dots in the Purcell regime using luminescence intensity autocorrelation. For measuring luminescence autocorrelations, I used two laser pulses with a controlled time delay to sequentially excite the coupled system and measured the emission as a function of the delay times and the laser powers. I found distinct contrasts between exciton and biexciton autocorrelations which originate from different nonlinearities. Finally, I performed a quantum optical simulation that accounts for the interaction between the laser pulses, exciton, and cavity mode to quantify the parameters related to the coupling.

1.3 Organization

This thesis is organized as follows. Chapter 2 introduces the optical properties and growth methods of quantum dots and describes some of the site-control techniques. In Chapter 3, I investigate the spatially resolved photoluminescence of InAs quantum dots patterned by a focused-ion-beam. Chapter 4 contains an introduction to photonic crystals including the origin of photonic bandgaps, the two different coupling regimes to a quantum dot, and the prospect of building a photonic network using photonic crystals. Chapter 5 describes computational methods to simulate a photonic crystal cavity and compares the calculated results with measurements. Chapter 6 explores the nonlinear dynamics of quantum dots coupled to a photonic crystal cavity in the Purcell regime. Finally, Chapter 7 summarizes this work and makes suggestions for future research.

Chapter 2

Semiconductor Quantum Dots

Quantum dots (QDs) are nanostructures that are small enough so that confined electrons (holes) can have discrete energy levels. Due to their rich quantum optical and electronic properties, QDs can be utilized for various applications from light emitting diodes [26], low-threshold lasers [27], solar cells [28] to single electron transistors [29] and quantum bits (qubits) [30] for quantum information processing. This chapter will introduce the quantum confinement effect of QDs and their subsequent optical properties. We will also look into how we can grow these semiconductor QDs epitaxially. The self-assembly method will be briefly introduced. Then various site-control methods will be reviewed with a special focus on focused-ion-beam patterning.

2.1 Quantum Confinement

Semiconductor heterostructures can be categorized as wells (2D), wires (1D) and dots (0D) depending on their dimensionality of spatial confinement. The effect of spatial confinement is that the movement of charge carriers is restricted to fewer dimensions. Therefore, the density of states, defined as the number of available electronic states per unit area per unit

energy, changes as shown in Fig. 2.1. For example, the electronic density of states in 3D bulk near the band edge energy (E_0) can be expressed as follows using the effective mass (m^*) approximation [31].

$$DOS_{3D}(E) = \frac{\sqrt{2}m^{*3/2}(E - E_0)^{1/2}}{\pi^2\hbar^3} \tag{2.1}$$

We can also obtain the density of states at lower dimensions as follows. Note the appearance of subbands due to the quantum confinement effect.

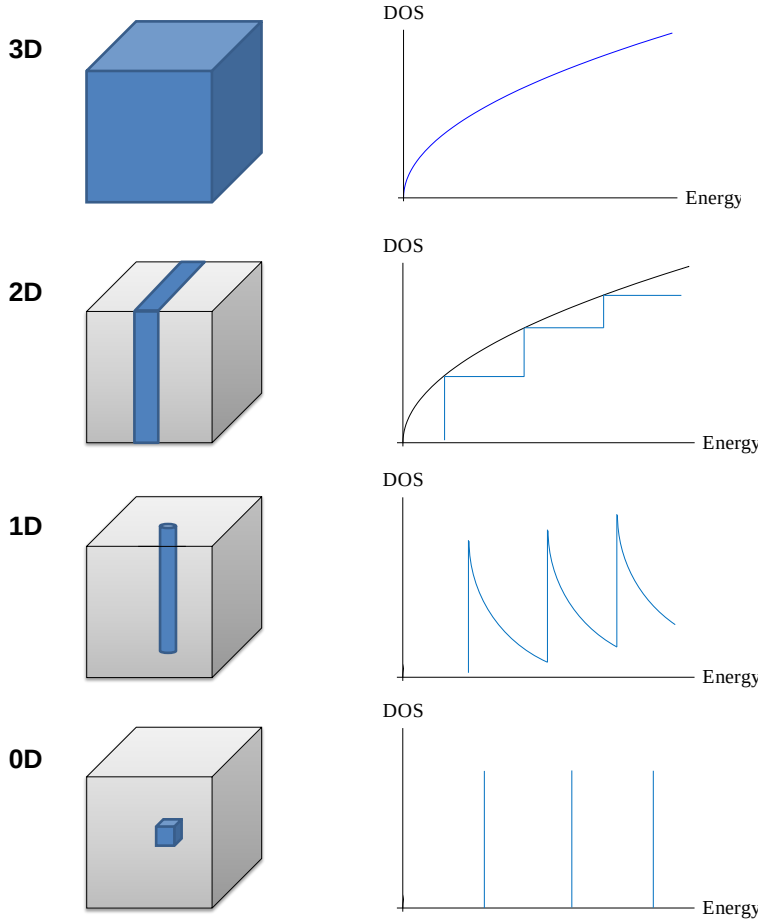

Figure 2.1: Density of states of low dimensional structures.

$$DOS_{2D}(E) = \frac{m^*}{\pi\hbar^2}; \qquad E > E_i \text{ for each subband.} \tag{2.2}$$

$$DOS_{1D}(E) = \frac{\sqrt{2}m^{*1/2}(E - E_0)^{-1/2}}{\pi\hbar}; \qquad E > E_i \text{ for each subband.} \tag{2.3}$$

The density of states at 0D becomes discrete as a result of spatial confinement in all three dimensions.

$$DOS_{0D}(E) = \delta(E - E_i) \tag{2.4}$$

The situation is similar to a particle in a box or an electron bound to a nucleus. Therefore QDs are sometimes called 'artificial atoms' for their discrete energy states. Although composed of hundreds to thousands of atoms, a QD can confine an electron (e), hole (h) or exciton (e-h pair) if the dot size is comparable or smaller than the exciton Bohr radius.

There are a few key differences between QDs and atoms. First, while atoms are all the same given the same atomic number and number of electrons, no two QDs are alike. This is due to complex microscopic processes involved during the fabrication of a QD that affect the QD's geometry, composition and environment. Therefore there has been a lot of efforts to control QDs using temperature [32] and field [33] tuning which is necessary to incorporate them as qubits for information processing. In addition, for solid-state technologies, highly tunable QDs at the fabrication level are attractive for various practical applications including light emitting diodes [26] and solar cells [28].

Another difference is that the excitons of QDs can be dissociated by thermalization at room temperature ($k_BT = 25.6$ meV) more easily than atoms due to a larger size and smaller binding energy (see Fig. 2.2), which is why cryogenics is generally required in QD experiments.

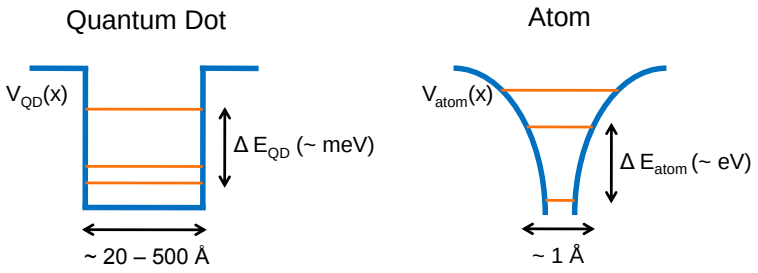

Figure 2.2: Energy level diagram of a quantum dot compared to an atom.

The epitaxially grown QDs are generally embedded in a substrate which has a larger bandgap than QDs. For example, InAs QDs are embedded in a GaAs substrate. Therefore the surrounding substrate can act as finite potential wells in all directions for an electron (hole) confined in a dot. By varying the width of the wells (size of the QD), one can tune their energy states.

2.2 Photoluminescence of quantum dots

The energy states of QDs can be optically accessed using photoluminescence measurements. When a sufficiently high energy is absorbed by a QD, an electron in the valence band can be excited to the conduction band and form an e-h pair which is called an exciton [Fig. 2.3].

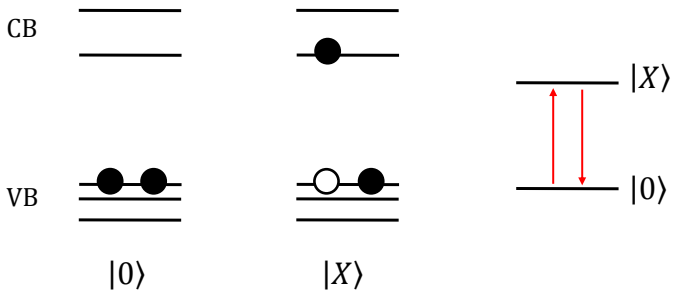

Figure 2.3: Ground and exciton states of a quantum dot. Photon absorption and emission can induce transition between the two states. CB and VB refer to conduction and valence band, respectively.

This e-h pair recombines after a characteristic lifetime and can produce spontaneous photon emission. Since the energy states of a QD are discrete, the emitted photon also has a very narrow spectral width. The photoluminescence spectrum measured from multiple self-assembled InAs QDs is shown in Fig. 2.4 at $T = 10$ K and when laser $P = 0.28$ μW using above-bandgap HeNe excitation ($\lambda = 633$ nm). The linewidth of single QD excitons varies between 0.05 nm (70 μeV) and 0.2 nm (300 μeV) due to different radiative recombination [34], spectral wandering [35–37], charge fluctuations [38] and pure dephasing [39].

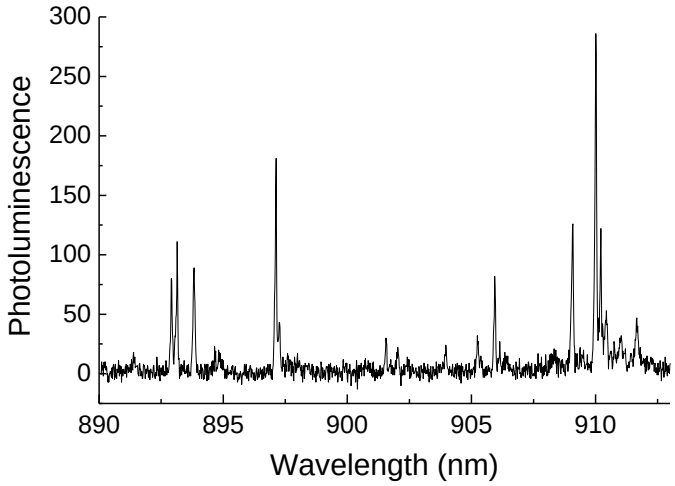

Figure 2.4: Micro-photoluminescence of individual quantum dots.

2.3 Growth Techniques

There are several types of QDs depending on growth methods. Colloidal type QDs [26] are synthesized from QD compounds dissolved in solutions which then nucleate to create nanocrystals at high temperatures. CdSe, CdS and InP QDs can be synthesized by colloidal methods and have direct applications in LED technology. Lithographically patterned QDs [40] are defined by gate electrodes etched on 2D electron gases in semiconductor heterostructures. Self-assembled QDs can be grown on a substrate using molecular-beam-

epitaxy (MBE). The QDs discussed in this thesis are grown by MBE, so let's take a closer look at the self-assembly method.

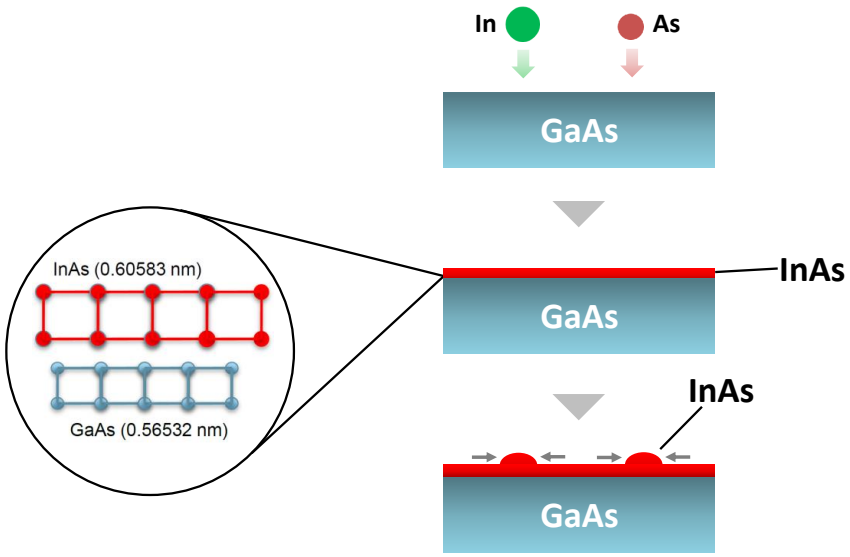

Figure 2.5: Molecular beam epitaxy (MBE) growth of self-assembled quantum dots.

Fig. 2.5 shows the schematic of growing InAs QDs by MBE method. In this method, a single crystal GaAs substrate is first grown in an MBE chamber under high vacuum. Then heated Indium and Arsenic gases are provided and condense on GaAs to form a single crystal InAs wetting layer. By increasing the thickness of the InAs wetting layer, strain energy starts to build up rapidly due to the lattice constant mismatch between InAs (6.06 $\mathring{A}$) and GaAs (5.65 $\mathring{A}$). In order to relieve the strain, InAs starts to nucleate and forms islands which are QDs. Such growth method is known as the Stranski-Krastanov method [41] or 'layer-plus-island' growth. The thickness of the wetting layer where QDs start to nucleate is called the 'critical thickness'. For InAs/GaAs QDs, the critical thickness is between 1.5 and 2.0 monolayers (ML) depending on MBE chamber conditions [42]. The size and density of QDs depend on the growth rate which can be controlled by temperature. The atomic force microscopy (AFM) image of an InAs QD sample is shown in Fig. 2.6.

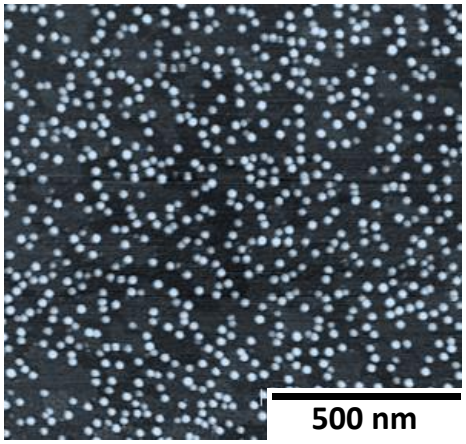

Figure 2.6: Atomic force microscopy (AFM) image of InAs quantum dots grown on GaAs substrate. Image courtesy of Timothy Saucer.

2.4 Site-controlled Quantum Dots

Epitaxially grown QDs typically nucleate at random locations as shown in Fig. 2.6. Such random positioning has been detrimental for some applications such as LED or solar cells which require a desired dot density and homogeneity. Additionally, integrating QDs to optical structures like a waveguide or cavity requires an accurate positioning of QDs for scalable quantum information processing. Therefore, there has been a lot of efforts to achieve site-controlled QDs using either a templating or etching method which are shown in Fig. 2.7.

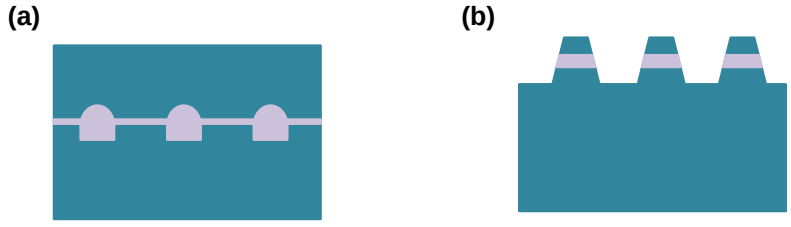

Figure 2.7: Site-controlling quantum dots. (a) Templating method (b) Etching method

In a templating method, QDs are formed at predetermined locations where holes are fabricated prior to the deposition of QDs. Various methods are developed to fabricate holes including electron-beam lithography [15–20], focused-ion-beam [21–23], local oxidation [24] and using crystal growth anisotropy [25]. Etching methods are also possible which create QDs by selectively etching the sample except the QD areas. Progress on fabricating GaN QDs using an etching method have been recently reported [43].

2.4.1 Focused-Ion-Beam

The site-controlled InAs QDs discussed in Chapter 3 of this thesis are grown by the focused-ion-beam (FIB) method. Here we review the FIB growth method performed by Andrew Martin before moving on to the details of the experiments.

FIB patterning during the QD growth process is shown in Fig. 2.8. First a GaAs layer is grown in a MBE chamber to prepare a substrate for growing QDs. Then this substrate is moved to the FIB chamber *in vacuo*. In this chamber, the substrate was exposed locally to a single pass of a 10 pA, 30 keV Ga^+ focused ion beam. The size of the holes can be controlled by the FIB dwell time. For example, the diameter and depth of the holes increase from 85 nm and 3 nm to 133 nm and 12 nm, respectively by increasing the FIB dwell time from 1 ms to 9 ms [44]. The 2D lattice spacing between the FIB patterns could also be controlled. After patterning the holes, the sample is moved back to the MBE chamber *in vacuo* to deposit single or multilayers of InAs QDs in addition to GaAs intermediate layers and a capping layer depending on sample designs. The single layer of FIB-induced InAs QDs image measured by AFM is shown in Fig. 2.9. QDs are formed only in the FIB exposed area. This is because the thickness of InAs was smaller than the critical thickness required to nucleate self-assembled QDs on the unpatterned surface. In the FIB hole area, the additional strain by the changed surface morphology has induced QDs to be selectively formed.

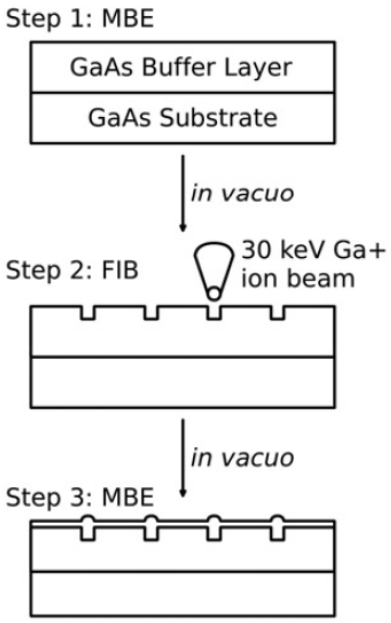

Figure 2.8: Focused-ion-beam-induced single quantum dots growth. Reprinted figure with permission from [45]. Copyright (2011) by Elsevier.

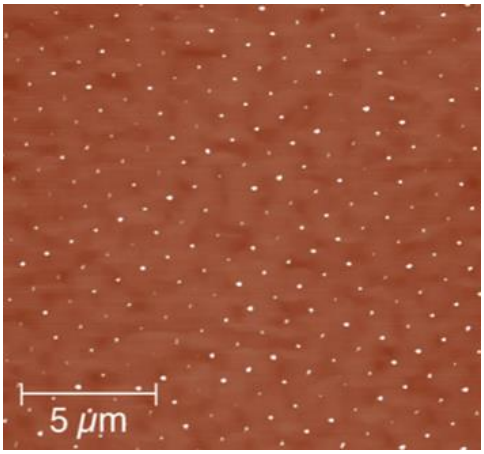

Figure 2.9: AFM image of a single layer FIB-induced QDs. FIB dwell time is 1 ms and 2.0 ML of InAs is deposited to form QDs. Reprinted figure with permission from [46]. Copyright (2013) by the American Vacuum Society.

2.4.2 Other Techniques

There are other techniques that have achieved site-controlling of QDs using templating methods in addition to FIB patterning. E-beam lithography and wet etching is one of the most widely used methods [15–20]. This method has shown an accurate placement of QDs [17] and the ability to generate single photons for qubit applications [47, 48]. More recently, QDs grown on an etched pyramidal substrate has demonstrated a highly symmetric QD growth which will be advantageous for polarization-entangled photon creation [49]. The pyramidal QDs has also shown that a deterministic coupling to photonic crystal cavities is possible [50, 51]. However, site-controlling QDs by etching requires a careful treatment of an etched surface before depositing QDs to prevent oxidation and contamination at the patterned sites which adds chemical steps in the fabrication process [19]. In contrast, the FIB method does not require these additional steps. Nevertheless, it has been known that the aforementioned techniques create defects at the QD sites which result in the line-broadening of single QDs which is undesirable when using QDs as qubits. To improve this issue, a new approach has recently been reported which induces defect-free site-controlled QDs on a nanoengineered substrate by using crystal anisotropy [25].

Chapter 3

Site-Controlled Quantum Dots using Focused-Ion-Beam

3.1 Motivation

Semiconductor quantum dots (QDs) have great potential for a wide variety of applications ranging from low-threshold diode lasers and solar cells to quantum bits for quantum information processing. Electron confinement in three spatial dimensions leads to discrete atom-like energy levels that can be tailored by changing the size and composition of the QD. However, self-assembled QDs typically nucleate at random locations, which is detrimental for some applications. For example, the coupling strength and Purcell enhancement of a QD in a photonic crystal cavity depends on the spatial and spectral overlap of the QD with the cavity mode [7, 12]. Therefore, there has been great interest in precisely controlling the locations and improving the spectral homogeneity of self-assembled QDs. This placement has recently been demonstrated using electron beam lithography [15–20] and focused-ion-beam (FIB) patterning [21–23] to produce preferred sites for QD nucleation.

E-beam pre-patterning has accurately positioned QDs to within 50 nm of their desired lo-

cations, as determined using scanning electron microscopy[17]. However, the patterned holes were observed to result in a broader single dot emission linewidth compared to unpatterned self-assembled dots [18]. The QD linewidth has been improved through better preparation of the patterned substrates [19] as well as vertical stacking of QDs above the initial layer of prepatterned dots [20].

FIB-patterning has also been shown to direct the nucleation of QDs at predetermined locations, as verified by atomic force microscopy (AFM) [21, 23]. In these experiments, growth on ion irradiated substrates leads to a reduction of the critical thickness for QD formation. Arrays of QDs have been achieved by growing upon substrates patterned with holes milled by the FIB. Photoluminescence (PL) measurements on ensembles of FIB-directed dots have demonstrated that they can be optically active [21, 23, 45]. However, single dot emission by FIB patterning had not yet been reported. Information about the spectral linewidth, homogeneity and accuracy of placement of individual FIB patterned optically active QDs is necessary to determine the possible range of application of this technique.

Here we report on optical measurements conducted on multi-layer stacks of FIB-patterned InAs QDs. We use scanning confocal microscopy to spatially map the PL of individual dots, giving a site-selective spectral probe of the dot luminescence. Single dot luminescence with 0.1 nm (160 μeV) linewidth is observed. We mapped an area containing 16 FIB-templated sites to characterize the fidelity and spectral homogeneity of optically active quantum dots at each site. We find that dots at the same site have similar emission wavelengths. These measurements show the potential for this technique to regulate the spectral and spatial homogeneity of site-controlled self-assembled InAs quantum dots.

The results described in this chapter have been published in Ref. [52] and [53].

3.2 Sample Fabrication

In vacuo FIB-patterning of GaAs was used for directed growth of a multi-layer InAs/GaAs QD structure [Fig. 3.1] by molecular beam epitaxy (MBE). A 300 nm GaAs buffer layer was grown at a substrate temperature of $T = 590$ °C after oxide desorption. The structure was then annealed for ten minutes under an As overpressure. The As and Ga fluxes for buffer growth were 2.8 and 1.0 monolayers s^{-1} (ML s^{-1}), respectively.

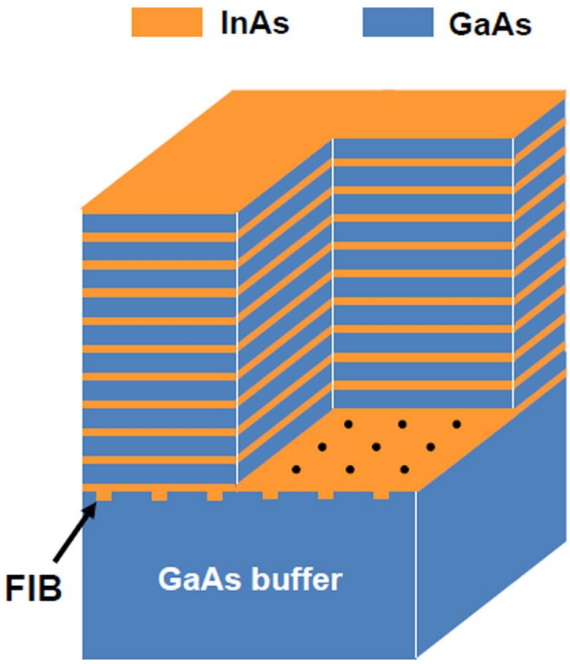

Figure 3.1: Sample schematic. Seed QD positions (black circles and arrow) are patterned by FIB in a square lattice of 2 μm spacing. 11 layers of 1.5 ML InAs QDs were subsequently deposited with 45 nm GaAs interlayers. Reprinted figure with permission from [53]. Copyright (2013) by Elsevier.

Next, the sample was transferred in vacuo to the FIB where a 40 x 40 μm^2 square array

was patterned. The array consisted of circular, FIB-milled holes spaced 2.0 μm apart in a 2D square lattice. Each hole was dosed in a single pass with a 9.2 pA, 30 keV Ga^+ ion beam with a dwell time of 3.0 ms. A similar array with the same spacing was also patterned on the same substrate using a shorter dwell time of 1.0 ms.

The sample was subsequently transferred back to the MBE chamber, where the sample temperature was raised to the growth temperature of $T = 485$ °C under an As overpressure. Eleven 1.5 ML-thick layers of InAs were grown at a rate of 0.11 ML s^{-1}, separated by 45 nm-thick GaAs spacer layers grown at a rate of 1.0 ML s^{-1}. The topmost layer of InAs remained uncapped. The As flux remained constant at 2.8 ML s^{-1} for both the QD and spacer layers. After growth of the eleventh layer of QDs, the sample was immediately quenched under an As overpressure. All substrate temperatures were determined using an optical pyrometer and all fluxes were determined by reflective high-energy electron diffraction oscillations.

AFM imaging of the FIB-induced structures showed the formation of QDs only in the patterned areas, in agreement with prior results [22, 23]. Previous experiments showed that these patterning conditions created holes that resulted in QD formation for deposited InAs thicknesses less than the critical thickness for self-assembled dots on unpatterned areas of the sample. AFM images of the uncapped surface confirmed dot formation upon stacking. Figure 1 shows AFM images of the sample in the patterned region where the FIB dwell time was 1.0 ms [Fig. 3.2 (a)] and an unpatterned region [Fig. 3.2 (b)]. The unpatterned region is devoid of QDs, as the critical thickness for their formation has not been exceeded. However, within the patterned region, QDs are visible and have the intended spacing of 2 μm. Observed dots are about 50-60 nm wide and 2-3 nm high. In addition to the QDs, mounds that are 0.3 by 0.6 μm in size are also present. The mounds are most likely a consequence of the strain introduced by patterning and subsequent overgrowth. Such mounds have also been observed in multilayer stacks of QDs grown on substrates patterned using e-beam lithography [54, 55].

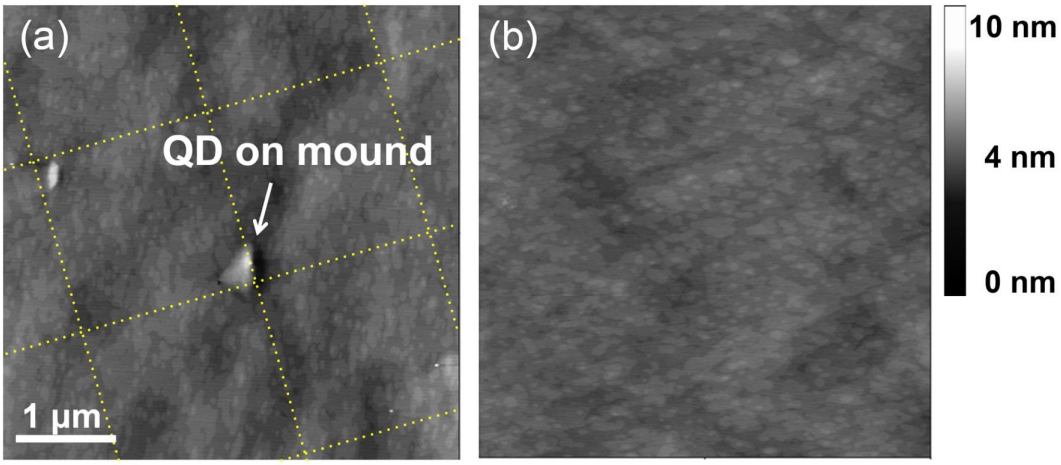

Figure 3.2: AFM images of patterned (a) and unpatterned (b) areas of a multilayer QD sample. The only difference in this sample and the area for which we report PL measurements is the shorter FIB exposure time (1.0 ms vs. 3.0 ms). Grid intersects in (a) represent the approximate locations of the FIB holes. Reprinted figure with permission from [52]. Copyright (2011) by the American Chemical Society.

3.3 Scanning Micro-photoluminescence Set-up

Spatially-resolved micro-PL measurements [Fig. 3.3] were conducted in a helium-flow cryostat for the optical characterization of the QDs. All spectra shown were taken at a temperature of 30 K unless otherwise noted. A continuous-wave HeNe laser (633 nm wavelength) was used to excite PL, with a typical excitation power of 0.4 μW measured before the cryostat. The excitation beam was focused onto the sample (5 μm beam diameter) using a 0.7 NA objective lens with 100X magnification. The same objective lens was also used to collect the PL, and a fast-steering mirror controlled the angle of the beam path going into and out of the objective lens for the 2D spatial mapping. The collection path included a lens pair and a 150 μm pinhole in a confocal microscopy configuration. After passing through a 0.75 m

spectrometer with a 1200 lines/mm reflection grating, the PL spectra were recorded by a CCD detector with 5 s exposure time.

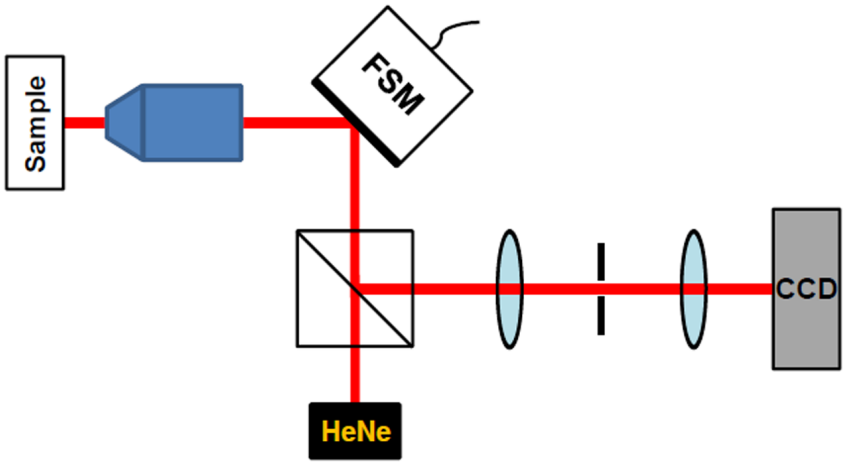

Figure 3.3: Scanning micro-PL set-up. Fast-steering-mirror (FSM) controls the spatial scanning electronically and confocal microscopy is employed in the PL collection path to increase the spatial resolution. Reprinted figure with permission from [53]. Copyright (2013) by Elsevier.

3.4 Optical Characterization Results

3.4.1 Single Quantum Dot Photoluminescence

Emission spectra from individual quantum dots were resolved using scanning micro-PL measurements [Fig. 3.4]. Single dot emission spectra centered at 891.1 nm was recorded at 30 K over an area of 4 x 4 μm^2 with 0.2 μm step size on the patterned region with 3.0 ms FIB dwell time. Fig. 3.4 (a) shows the spectrum measured at the position where the dot luminescence is strongest. The single dot emission spectrum has a full-width at half-maximum (FWHM) of 0.1 nm (160 μeV). The FWHM of single dots measured in this sample were all below

0.2 nm (300 μeV). These relatively narrow linewidths indicate that the dots are sufficiently isolated from surface states and charge traps that may have been introduced by the FIB milling and could introduce additional nonradiative relaxation pathways or contribute to dephasing and spectral diffusion [18, 56]. The inset shows the temperature dependence of the emission wavelength, which shifts as expected due to the band gap change of the InGaAs material [57]. Within this temperature range (10-50 K), there was no significant increase in the measured linewidth. The power selected for these measurements (0.4 μW) was below the threshold power where excited state emission is expected. A power dependence measurement showed that the QD emission increased linearly with power between 0.04 μW and 0.43 μW and saturated at higher power. We did not observe any emission from dots away from the patterned region.

Fig. 3.4 (b) shows the spatial map of the PL at wavelength 891.1 nm. The pinhole size of 150 μm was selected for the imaging based on the trade-off between resolution and signal loss. Assuming the Airy disc-like pattern of the beam, the theoretical pinhole size limited lateral and axial resolutions of the image are 0.5 μm and 1 μm, respectively [58]. In our measurements, the lateral resolution is approximately 1 μm [Fig. 3.4 (c)]. Since the minimum possible axial resolution due to the pinhole (1 μm) is larger than the structure thickness (11 stacks with a total thickness of 450 nm), we cannot easily determine the layer from which the dot emission originates from the measurements. However, the center of the QD emission can be determined with greater accuracy than the lateral resolution by fitting the QD emission and collecting statistics from multiple scans [59].

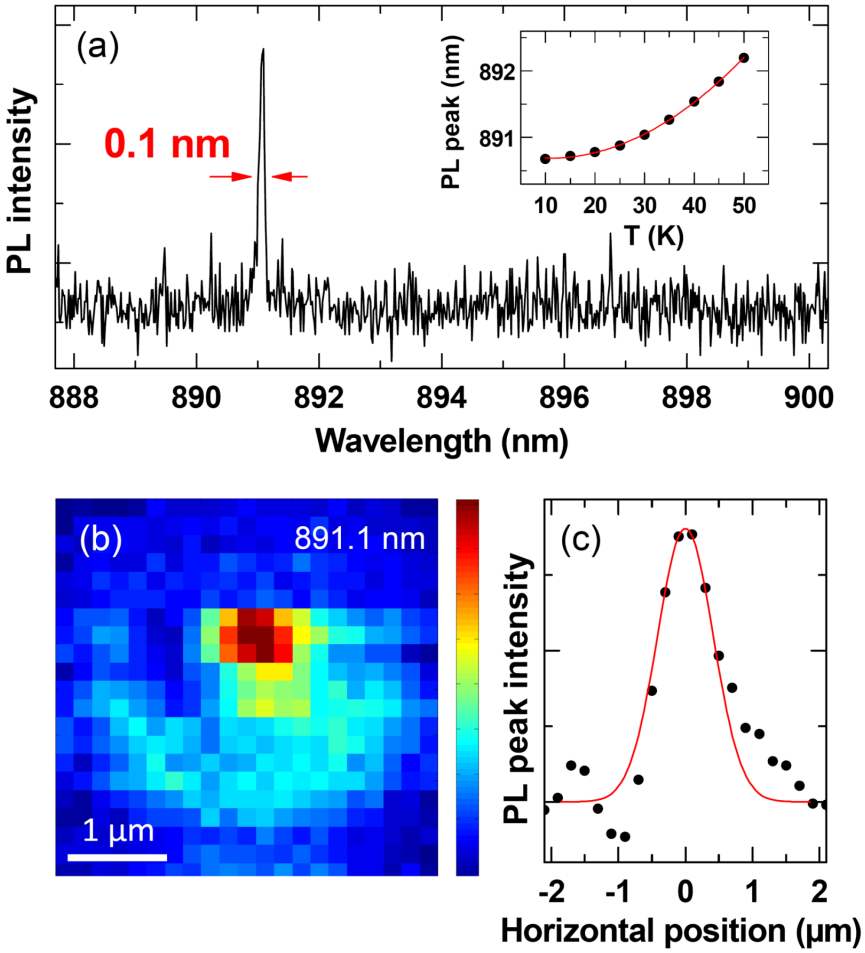

Figure 3.4: Spectrally and spatially resolved single dot PL from FIB-patterned InAs/GaAs QD sample. (a) Single dot PL measured at $T = 30$ K. FWHM of 0.1 nm (160 μeV) is observed. The inset shows the temperature dependence of the PL peak wavelength (black circles) and a second order polynomial fit (red line). (b) 2D spatial map of PL intensity at 891.1 nm. (c) 1D line scan through the center of the PL peak, showing a spatial resolution of 1 μm as determined by a Gaussian fit (red line). Reprinted figure with permission from [52]. Copyright (2011) by the American Chemical Society.

3.4.2 Power Dependence of Single Quantum Dot

In Fig. 3.5, we present a power dependence measurement of a single QD and the wetting layer for comparison. While increasing the excitation power from 4 nW to 2000 nW, we recorded the emission spectrum from 800 nm to 1000 nm.

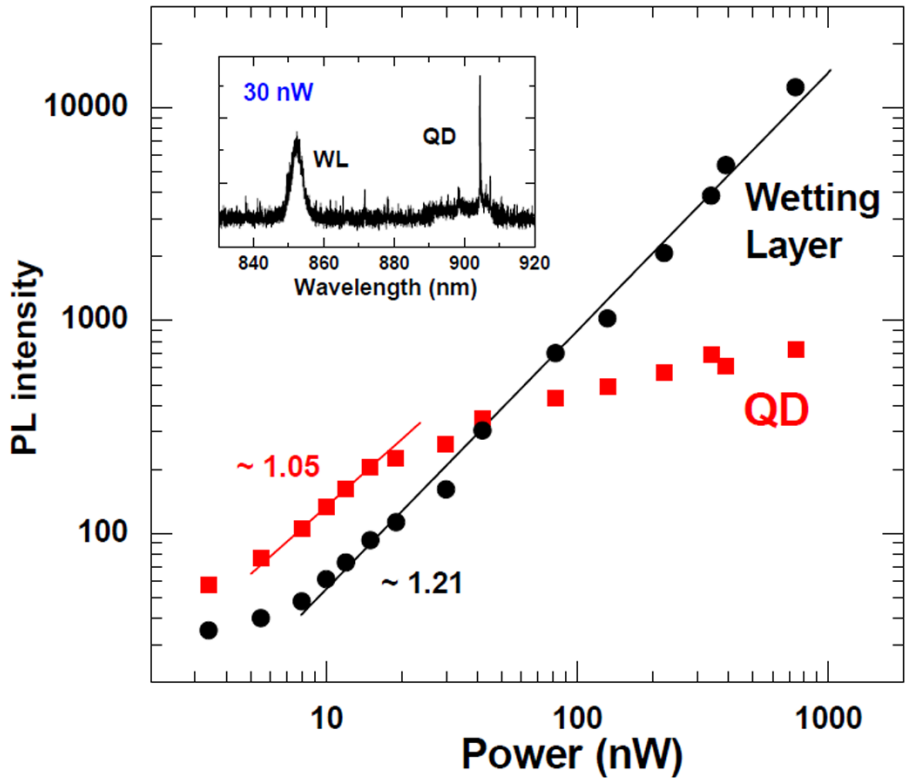

Figure 3.5: The power dependence measurement of a single QD and the wetting layer (WL). The PL intensity is the recorded peak intensity of the QD and WL peaks, respectively, measured as a function of power at the sample, from 4 nW to 2000 nW. The inset shows the spectrum recorded at 30 nW. Reprinted figure with permission from [53]. Copyright (2013) by Elsevier.

The QD emission increases nearly linearly and then saturates as a function of pump

power, which is consistent with single exciton emission by a single photon emitter. For this spectral window and range of excitation powers, we did not observe excited state emission. The absence of excited state emission may be due to the emission wavelength of ground state excitons ($\sim$ 900 nm) being close to the bandgap of GaAs ($\sim$ 855 nm), resulting in not sufficiently strong excited state confinement. It should be noted that similar measurements were done on three different QDs at different locations, which showed the same behavior.

3.4.3 Spatial Imaging of Site-controlled Quantum Dots

In order to determine the relative placement of the QDs, we then mapped the PL over a 6 x 6 μm^2 region containing multiple dots using a 0.2 μm step size. For this measurement, we collected spectra from wavelength of 890 nm to 910 nm. Fig. 3.6 (a, b, c, d) are intensity profiles of the same region for wavelengths 902.0 nm, 902.8 nm, 898.8 nm, and 899.2 nm, respectively. Fig. 3.6 (e) shows the PL spectra at the selected positions labeled A, B, and C. Single dot PL centered at 904.8 nm was also localized around position B but is not shown here. It should be noted that at least four dots (898.8 nm, 902.0 nm, 902.8 nm, and 904.8 nm) are formed within 0.4 μm from locations A and B while two (898.8 nm and 899.2 nm) are formed within 0.2 μm around position C. In addition, we observed two dots with the same wavelength at 898.8 nm that are spaced 2.5 μm apart [Fig. 3.6 (c)], a distance close to the FIB-milled hole separation of 2 μm.

In order to verify that the dots are located on the FIB pattern, we later performed a spatial scan over a larger area and spectral range. The data presented in Fig. 3.8 was collected during a different cool-down than the data in Fig. 3.6 and after rotating the orientation of the sample in the cryostat in order to better align the underlying FIB pattern with the principal axes of the fast-steering mirror.

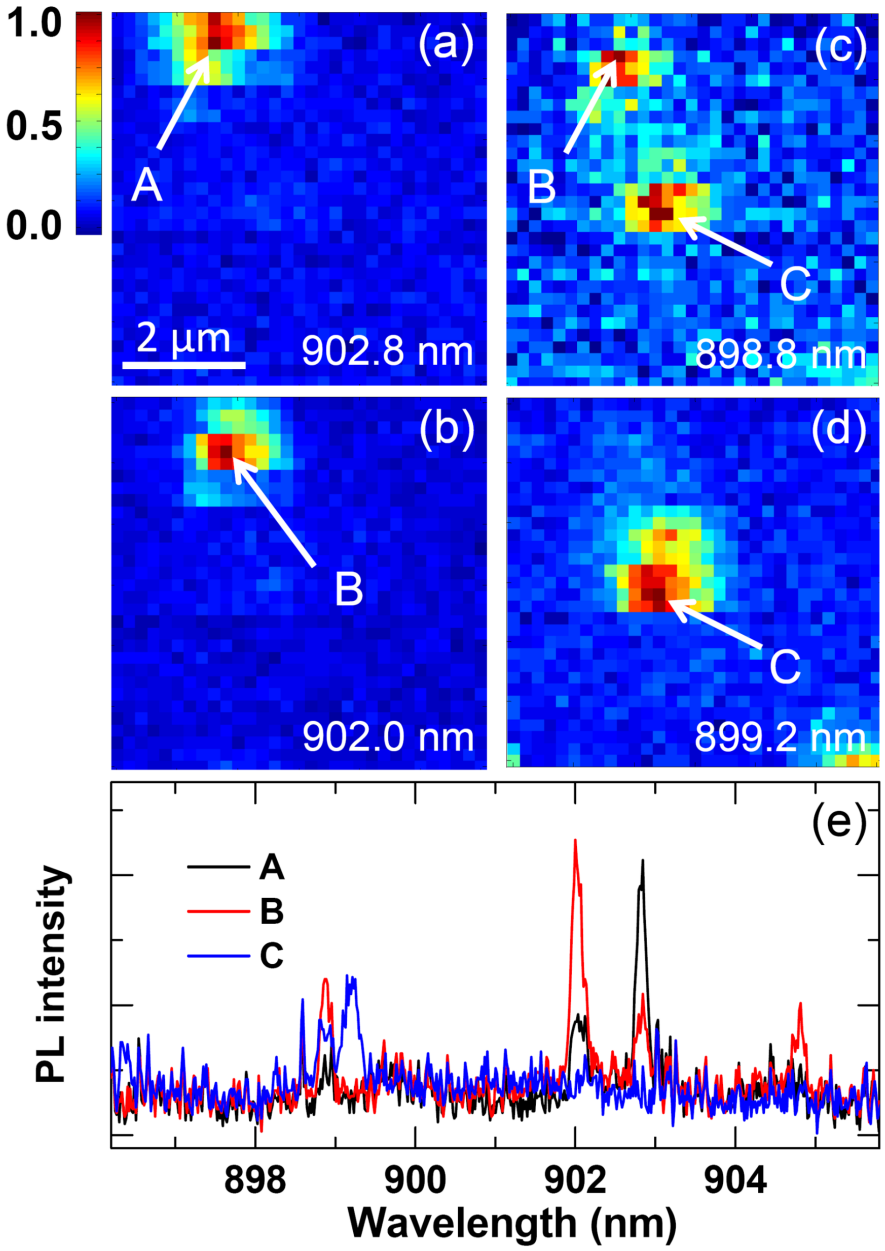

Figure 3.6: 2D PL intensity maps of the same spatial region at four different wavelengths (a, b, c, d) and PL spectra (e) at positions marked A, B, and C. Each map is separately normalized so that the color axis shows the relative intensity at each wavelength as a function of position. Note that two dots of similar wavelength are formed within a lateral separation of 0.4 μm: 902.8 nm and 902.0 nm at positions A and B, respectively and similarly 898.8 nm and 899.2 nm at position C. Reprinted figure with permission from [52]. Copyright (2011) by the American Chemical Society.

3.4.4 Multiple Emissions at the Same site

Before we map a larger area for statistical analysis, let us focus on the reason why we observe multiple emission peaks at the same site. Multiple dot emissions (A - D) at the same location are observed in Fig. 3.7, while recording the spectra over a wavelength range from 870 nm to 950 nm. For each transition wavelength (A: 897.5 nm, B: 921.4 nm, C: 923.2 nm, and D: 924.2 nm), a PL intensity map scanned over the same area (6 x 6 μm^2) shows the spatially localized dot emission (inset). The black squares in the inset indicate the position where the depicted spectrum is measured. These multiple transitions at near sites could have originated from either different exciton transitions of the same QD or several different QDs from the stacked layers.

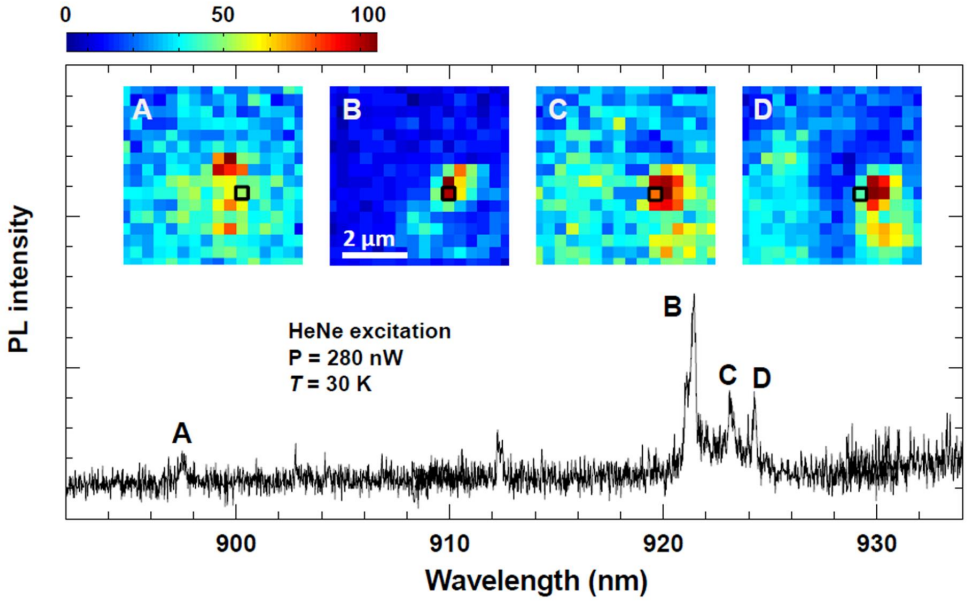

Figure 3.7: QD emission spectrum measured at one site. Multiple emissions are labelled by letters (A - D) and their PL maps at the corresponding wavelengths are shown in the insets. Each map is separately normalized so that the color axis shows the relative intensity at each wavelength as a function of position. All spectra are measured with 280 nW of HeNe excitation and at the temperature of 30 K. Reprinted figure with permission from [53]. Copyright (2013) by Elsevier.

If the multiple peaks originate from the same QD, the different exciton transitions could possibly be attributed to either (i) ground and excited state excitons, or (ii) neutral and charged excitons. However, the excited state emissions did not appear in this sample under our measurement conditions, and therefore all emissions are from the ground states, excluding possibility (i). In addition, from the PL maps shown in Fig. 3.7, the strongest emission peak position is not the same for maps A - D and slightly deviated (0.4 - 0.8 μm) from each other. From this lateral separation of PL positions, we exclude the second possibility as well. Therefore, the observed multiple peaks at near locations are from separate QDs which could be in the same layer or different layers. Since multiple dots could be formed at a single hole position in the initial layer as observed in the AFM image of similar samples [23], there is a possibility that some of the peaks are from dots in the same layer. However, by varying the axial position of sample relative to the focused laser spot in our measurement, we could observe changes in the relative intensity of peaks A - D (not shown), which is a strong indication that these dots are located in different layers. From these observations, we confirm that the multiple emissions are not from the same QD, but from several different QDs, some of which are vertically separated.

3.4.5 Statistical Results

A larger area 2D PL scan of the sample was conducted while recording spectra over a larger wavelength range, from 870 nm to 950 nm, in order to conduct statistical analysis on the placement and emission wavelengths of optically active QDs. A total of 26 optically active dots were observed over 16 array sites and the spectral inhomogeneity of the measured dots was approximately 20 nm (30 meV) [Fig. 3.8 (b)]. In Fig. 3.8 (a), the filled circles indicate the center positions of QD PL and the QD wavelength, as indicated by the color scale. The location of the QDs reflects the 2 μm square array of holes milled by the FIB. While AFM measurements have established that the hole diameter is around 100 nm for 3.0 ms FIB dwell

time, we observe that these QDs are more disordered than the original pattern, perhaps due to the fact that the observed mounding (see Fig. 3.2 (a)) shifts the dot position [54, 55]. The apparent scatter in the QD position is approximately 0.4 μm from the estimated center positions of the FIB pattern, which is on the same order as the size of the mounds. Note that multiple dots with similar wavelength tend to form near each other, consistent with our earlier observations for the dots in Fig. 3.6 and Fig. 3.7.

Fig. 3.8 (c) shows the frequency of occurrences of array sites containing a particular number of optically active dots, as observed in the micro-PL measurements and within 0.4 μm from the estimated site positions. At least 65 percent of sites contained optically active dots, and the maximum number of quantum dots detected at one site (four) was smaller than the total number of stacks (eleven). However, we anticipate that the initial and final (uncapped) layers of dots may have lower luminescence due to ion damage and surface states, respectively. In addition, the stacking fidelity may be low due to the somewhat large interlayer GaAs thickness [60]. Due to the limited axial resolution of this measurement, we cannot determine whether the observed multiple emissions at some sites are from dots formed on different layers or the same layer. AFM studies on uncapped dots have shown that multiple QDs may form at a single patterned hole [23]. However, we also noticed that the closely spaced QDs have similar wavelengths, indicating that they may have similar sizes. Cross-sectional imaging of stacked dots on a patterned sample have reported similar sizes within a stack [61].

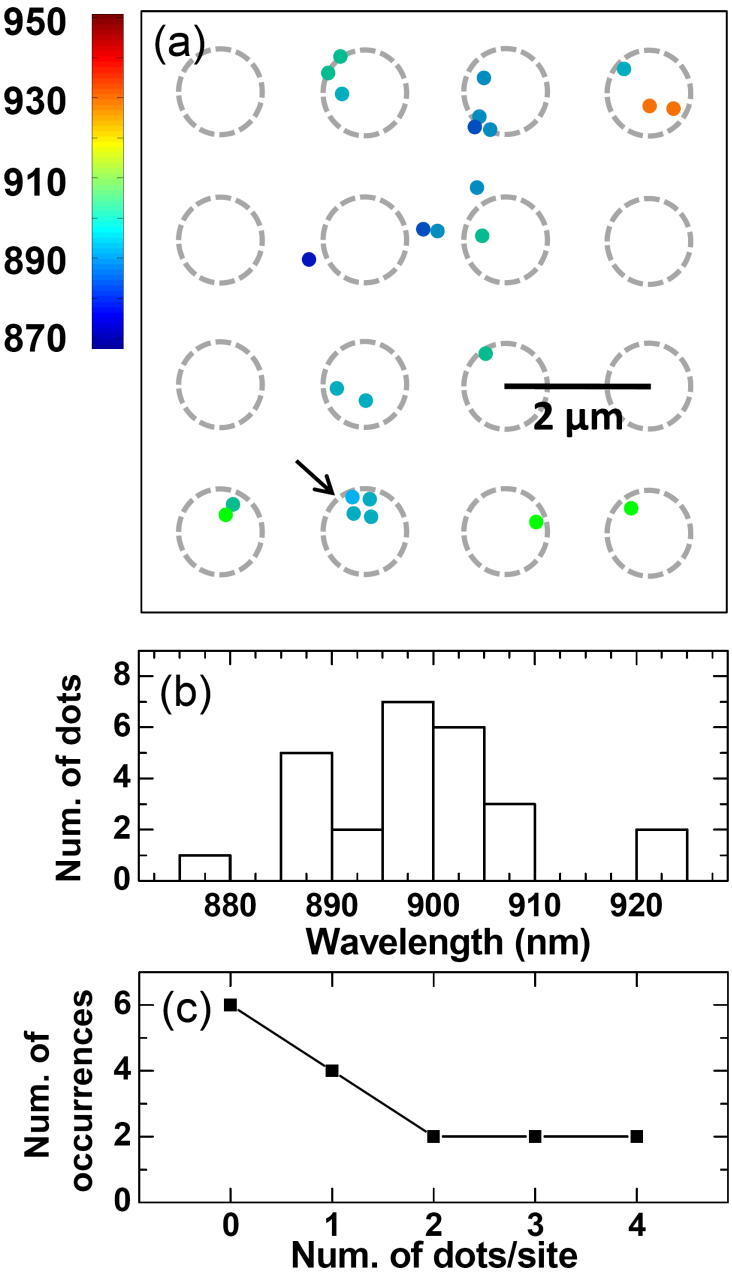

Figure 3.8: (a) 2D map of single dot PL over an 8 x 8 μm^2 area. The filled circles indicate the center positions of QD PL and the QD wavelength as indicated in the color bar. Estimated positions of the FIB holes are at the center of the dashed gray circles. The circles (0.4 μm radius) are our estimate of the site area. Note that multiple dots with similar wavelength can be formed at the same site (arrow). (b) Wavelength distribution of the QDs. (c) Number of occurrences of sites containing the specified number of dots. Reprinted figure with permission from [52]. Copyright (2011) by the American Chemical Society.

3.5 Conclusions

In summary, the first site-selective optical measurement is performed on FIB-patterned QDs using scanning micro-PL spectroscopy. Single dots of narrow linewidth (< 300 μeV) are observed with positions that reflect the lateral separation of the underlying FIB hole array spacing. Multiple dots at the same site have similar wavelengths, reflecting the size homogeneity of stacked dots. The observed position of the dots with respect to the initial FIB hole position may be shifted during the growth of the multilayer stack due to the formation of mounds. We expect that the shift in dot position may be reduced by varying the growth conditions and sample structure, and that the fidelity may be increased by decreasing the interlayer thickness. Our method images quantum dots with close to the diffraction-limited spatial resolution, which is advantageous for determining the center position of the dots. With abilities to position and spectrally probe and locate quantum dots, we anticipate the possibility of coupling multiple quantum dots in a network of photonic cavities, which is a promising pathway for the scalable integration of solid-state quantum bits.

Chapter 4

Photonic Crystals

Photonic crystals are nanostructured materials with periodic variation of dielectric constants. These crystals can create a range of forbidden frequencies called a photonic bandgap, similar to an electronic bandgap in atomic crystals of a semiconductor. Since photons with energies within the bandgap cannot propagate through the medium, photonic crystals can manipulate the light path and the density of optical states locally by introducing defects that can guide, bend and confine light. One such example is a 2D photonic crystal defect cavity which can localize light within a space smaller than a cubic optical wavelength. This chapter will introduce the origin of the photonic band gap of these structures and discuss the phenomena observed when quantum dots are coupled to photonic crystals. Also, the possibility of building a photonic network on a chip using quantum dots and photonic crystals will be briefly discussed.

4.1 Photonic Bandgap

To understand the photonic bandgap of periodic materials, we first look into the most simple case of 1D photonic crystals which are also known as distributed Bragg reflectors (DBR).

As an example, we show a periodic structure in Fig. 4.1 and compare it to a homogeneous material. The grey color is assumed to be GaAs ($\varepsilon_r = 12.9$) while empty spaces represent air ($\varepsilon_r = 1$). The ratio between the length of the air space (d) and the periodicity (a) is chosen to be 0.8 for the case of DBR. With these structures, we calculated dispersion relations using the plane wave expansion method [62]. Below we briefly show the basic principles of 1D plane wave expansion method.

In the plane wave expansion method, the electric fields and dielectric permittivities (ε_r) are expanded in Fourier series components along the reciprocal lattice vector.

$$\frac{1}{\varepsilon_r} = \sum_{m=-\infty}^{\infty} A_m^{\varepsilon_r} e^{-i\frac{2\pi m}{a}z} \tag{4.1}$$

$$E(\omega, \overrightarrow{r}) = \sum_{n=-\infty}^{\infty} A_n^{E_y} e^{-i\frac{2\pi n}{a}z} e^{-i\overrightarrow{k}\cdot\overrightarrow{r}} \tag{4.2}$$

Here we assumed that light propagates in the z direction along the material periodicity and the polarization of light is along the y-axis.

It is well known that under the plane wave assumption, Maxwell's equations can be combined to result in the following expression.

$$\frac{1}{\varepsilon(\overrightarrow{r})}\nabla \times \nabla \times E(\overrightarrow{r}, w) = (\frac{\omega}{c})^2 E(\overrightarrow{r}, w) \tag{4.3}$$

Substituting Eq.4.1 and 4.2 to 4.3, we obtain the following simplified form of an eigenvalue problem.

$$\sum_n (\frac{2\pi n}{a} + k_z)(\frac{2\pi m}{a} + k_z) A_{m-n}^{\varepsilon_r} A_n^{E_y} = (\frac{\omega}{c})^2 A_m^{E_y} \tag{4.4}$$

Solving this equation, we calculate the eigenvalues corresponding to the modal solutions and the results are shown in Fig. 4.1 when (a) d/a = 0 and (b) d/a = 0.8.

Introducing a periodicity to bulk GaAs has led to an important change in the photonic band structure. While the dispersion relation is linear in a homogeneous material, inserting periodic air gaps in the material has opened up gaps in the dispersion relation. This we can understand by the plane wave solutions satisfying the periodic conditions when $k = \pm\pi/a$ ($\lambda = 2a$). Due to the periodicity of the material permittivity, the eigenvector solution of Eq.4.4 has the form of stationary waves which has anti-nodes at either the center of GaAs or the air gaps. However, the energies (frequencies) of the two solutions are not identical due to the different energy density distributions ($\varepsilon_{air}E^2$ vs. $\varepsilon_{GaAs}E^2$), which opens up a gap. Therefore a material with a periodic dielectric contrast has photonic bandgaps.

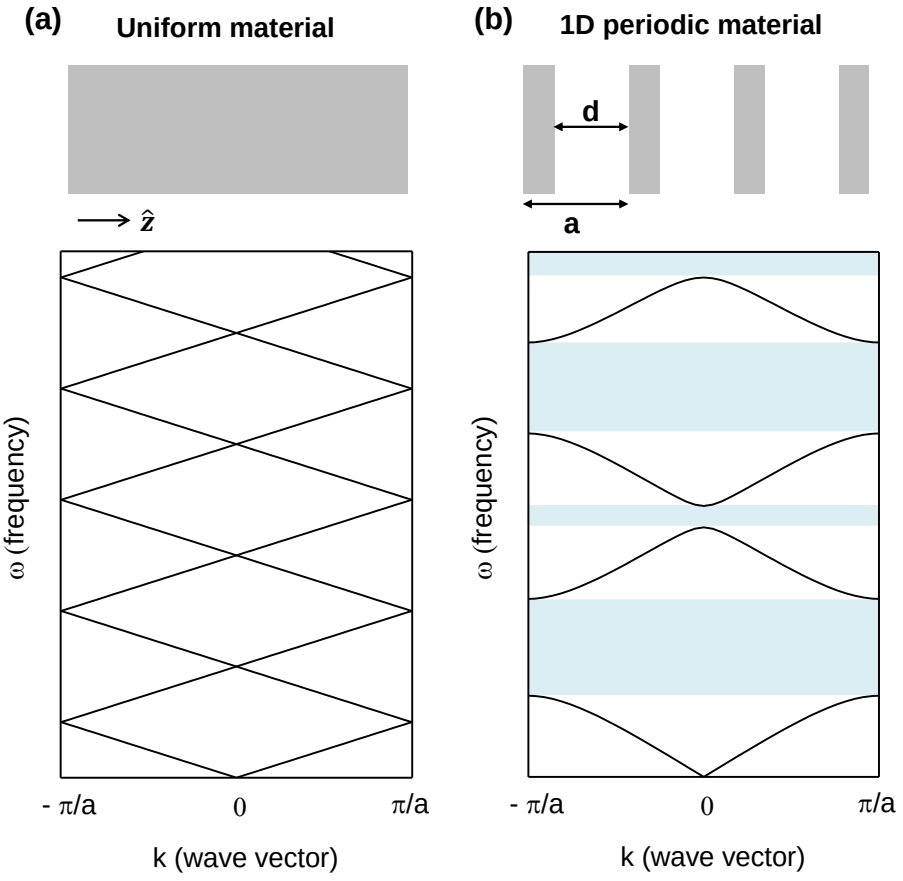

Figure 4.1: (a) Uniform material dispersion relation ($\varepsilon_{GaAs} = 12.9$). (b) 1D photonic crystal dispersion relation when d/a = 0.8 and $\varepsilon_{air} = 12.9$.

The same principle can be extended to 2D photonic crystals. One example is air holes placed in 2D hexagonal lattices as shown in the inset of Fig. 4.2. Due to the spatial periodicity of ε_r, dispersion relation is again different from a uniform material. The dispersion relation is calculated by Reference [63]. In 2D crystals, dispersion relation becomes anisotropic, therefore, we define three most symmetric points (Γ, M, K) in the reciprocal space and look into the dispersion relations on the line connecting these points.

One can also find that the modes are classified to either TE or TM modes. This is because of the mirror symmetry of 2D photonic crystals. Defining the in-plane of the photonic crystals as xy-plane, the operation $\widehat{z} \rightarrow -\widehat{z}$ must always give *even* or *odd* solutions. With this, the only non-zero components of *even* modes are (E_x, E_y, H_z) and that of *odd* modes are (H_x, H_y, E_z). The former confines E-fields in the xy-plane (TE modes) and the later confines H-fields in the xy-plane (TM modes). Note that these hexagonal air-hole type 2D photonic crystals prefer a bandgap in TE modes, but a complete bandgap can also appear when the size of the air holes becomes large enough.

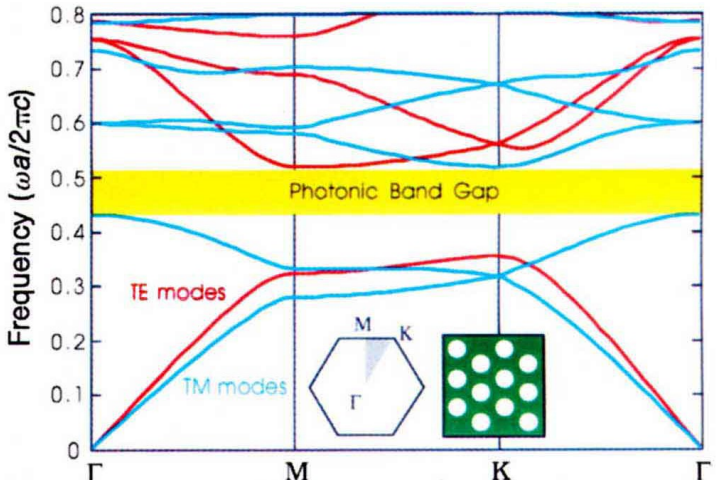

Figure 4.2: Dispersion relation of a hexagonal photonic crystals with air holes ($r = 0.48a$) in dielectric ($\varepsilon_r = 13$). For this large size of air holes, a complete bandgap can appear for both TE and TM modes. Calculation and image courtesy of reference [63]. Copyright (1997) by the Nature Publishing Group.

4.2 Photonic Crystal Cavity

We have seen that in a photonic bandgap, no photon modes are allowed. Therefore if light at the bandgap is shone onto or emerged in perfect photonic crystals, it can exist only evanescently and will decay exponentially. However, if we introduce a defect in the photonic crystal, the defect region can now sustain non-evanescent fields. Therefore this defect region can work as a cavity that can confine light. One such example is the $H1$ (or $L1$) cavity in Fig. 4.3 where defect is just a missing hole (the region where a QD is embedded). While the lateral confinement of light in this cavity originates from photonic crystals, the vertical confinement is achieved by the finite thickness of the slab through total internal reflection.

The figure of merit that shows the strength of the field confinement in a cavity is Q/V_{mode} where V_{mode} is the modal volume of the cavity

$$V_{mode} = \frac{\int \varepsilon(\overrightarrow{r})|\overrightarrow{E}(\overrightarrow{r})|^2 d^3\overrightarrow{r}}{max(\varepsilon(\overrightarrow{r})|\overrightarrow{E}(\overrightarrow{r})|^2)} \tag{4.5}$$

and Q is similar to the lifetime of the confined photons and thus inversely related to the decay rate of the cavity mode ($Q = \pi f_o/\kappa$). Note that Q depends on several factors including the lateral and vertical confinements and for realistic materials on material absorption and light scattering.

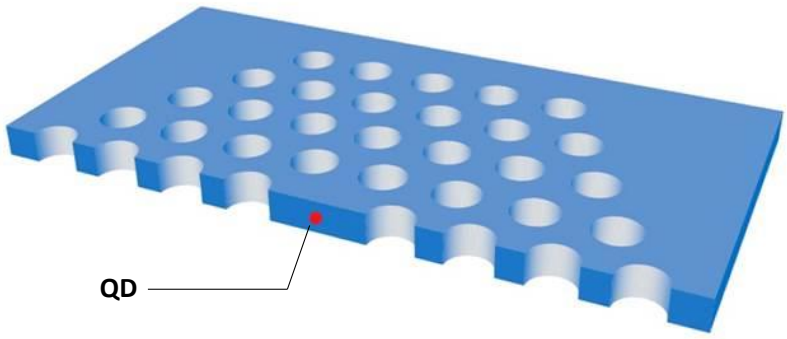

Figure 4.3: Schematic of H1 cavity with an embedded QD.

4.3 Coupling Quantum Dots to a Photonic Cavity

Photonic crystal cavities coupled to single QDs are an interesting platform to study light-matter interactions in solid-state systems and to develop a quantum network for information processing using photons. The advantage of photonic crystals is that current semiconductor technology can realize the coupling in a relatively simple manner compared to the more traditional atom-cavity interaction. However, most of the theory describing the coupling dynamics is borrowed from atomic cavity quantum electrodynamics (cQED) [64].

Fig. 4.4 shows the parameters governing the coupling between a QD and cavity. Here g is the coupling rate between the two, and κ and γ are the decay rates of the cavity and QD, respectively. Depending on the relative strength between the coupling and decay rates, the dynamics become dramatically different. When decay rates are larger than the coupling ($\kappa, \gamma > g$), the system is known to be in the Purcell regime and the spontaneous emission rate of the QD changes. In the opposite case (strong coupling), the coupling exceeds the decay rates ($\kappa, \gamma < g$) and the QD and cavity are coherently coupled and reversibly exchange energy with each other.

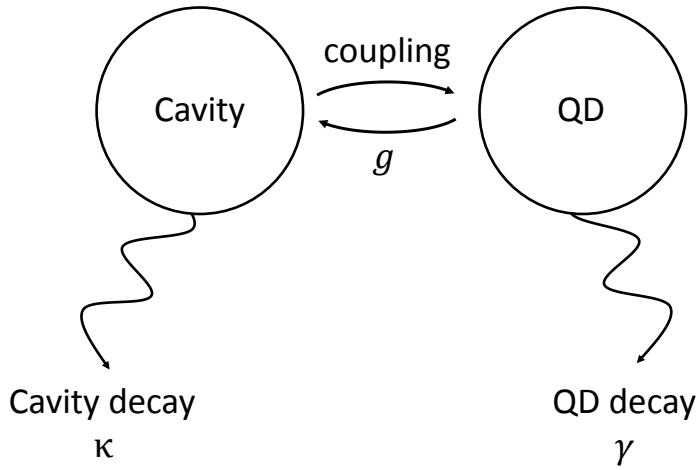

Figure 4.4: Schematic of QD-cavity coupling with dissipation.

4.3.1 Purcell Enhancement of Spontaneous Emission

The Purcell effect refers to the phenomenon where the spontaneous emission rate changes by modifying the emitter's optical environment [65]. In the theory of spontaneous emission, the emission rate is not an intrinsic property of a material but rather depends on the optical environment where the level transition accompanying the emission occurs.

The spontaneous emission rate of an emitter by transition from an excited state ($|e\rangle$) to a ground state ($|g\rangle$) can be derived using the Wigner-Weisskopf theory [66] which we describe here briefly. In the theory, the general state vector including all possible optical states k is given by

$$|\psi(t)\rangle = c_e(t)e^{-i\omega_o t}|e, \{0\}\rangle + \sum_k c_{gk}(t)e^{-i\omega_k t}|g, \{1_k\}\rangle \tag{4.6}$$

By substituting this in the Schrödinger equation $|\dot{\psi}(t)\rangle = -(i/\hbar)H_{int}|\psi(t)\rangle$ where $H_{int} = \hbar\sum_k(g_k\sigma^+ a_k + h.c.)$, one can get the probability that the emitter is in the excited state $P_e(t) = 1 - \sum_k |c_{gk}(t)|^2$. By calculating $P_e(t)$ and substituting $g_k = \sqrt{\omega_k/2\hbar\varepsilon_0 V}\mu_{12}$, we can get the excited state decay equation.

$$\frac{dP_e(t)}{dt} = -\frac{\omega^3|\mu_{12}|^2}{3\varepsilon_0\pi\hbar c^3}P_e(t) = (\frac{2\pi}{\hbar^2})|\langle\mu_{12}E\rangle|^2 D_{free}(\omega)P_e(t) = -\Gamma P_e(t). \tag{4.7}$$

The third term indicates that the spontaneous emission rate depends on both the material transition rate (μ_{12}) and the density of optical states in free space ($D_{free}(\omega)$), which corresponds to Fermi's golden rule.

If the emitter is placed inside a cavity, the density of optical states becomes

$$D_{cav}(\omega) = \frac{\kappa}{2\pi V_{mode}}\frac{1}{(\kappa/2)^2 + (\omega_{cav} - \omega)^2}. \tag{4.8}$$

By using this and the relation $Q = \pi f_0/\kappa$, we arrive at the expression of the final spontaneous emission rate of an emitter in a cavity at resonance.

$$\Gamma_{cav} = \Gamma_{free} \frac{3Q}{4\pi^2} (\frac{\lambda_0^3}{V_{mode}}) \tag{4.9}$$

The enhancement factor $\frac{3Q}{4\pi^2}(\frac{\lambda_0^3}{V_{mode}})$ is known as the Purcell factor (F) which is the possible maximum enhancement when the emitter is at resonance and perfectly placed and oriented inside a cavity. In reality the actual enhancement is smaller than F due to the spectral, spatial and polarization mismatches between the emitter and cavity.

$$\frac{\Gamma_{cav}}{\Gamma_{free}} = F \frac{\Delta\omega_c^2}{4(\omega_e - \omega_c)^2 + \Delta\omega_c^2} \frac{|\vec{E}(\vec{r})|^2}{|\vec{E}_{max}|^2} (\frac{\vec{d} \cdot \vec{E}(\vec{r})}{|\vec{d}||\vec{E}(\vec{r})|})^2 \tag{4.10}$$

4.3.2 Strong Coupling

When the emitter is strongly coupled to a cavity, the situation becomes quite different from the Purcell regime.

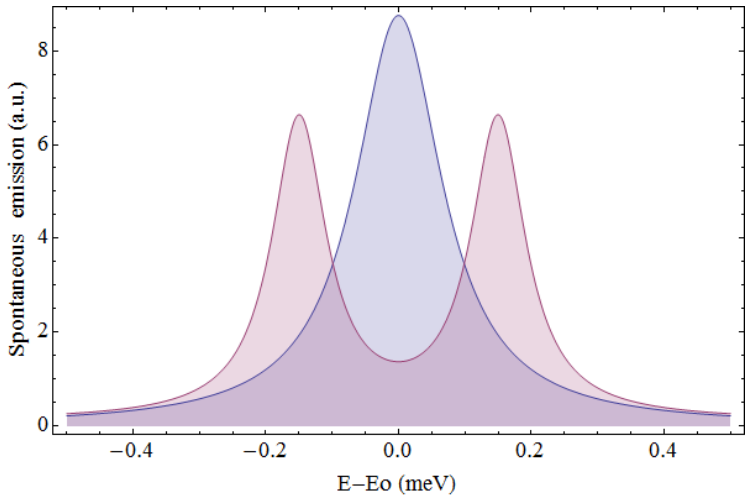

Figure 4.5: Schematic spontaneous emission spectrum of Purcell regime (blue) and strong coupling regime (red) at resonance.

Here the emitter and cavity form a polariton where the two entities mix together producing the level splitting in the emission spectrum at resonance. Such level splitting is the fingerprint of strong coupling and can be observed when the emitter is coupled to an extremely high Q (low κ) cavity. For a QD inside a photonic crystal cavity, for example, strong coupling can be observed when $Q > 3{,}000$ [67].

4.4 Toward Solid-State Photonic Network

The ability to fabricate QD-cavity coupled systems on a large scale using solid-state technologies is a promising route to build future photonic networks on chip.

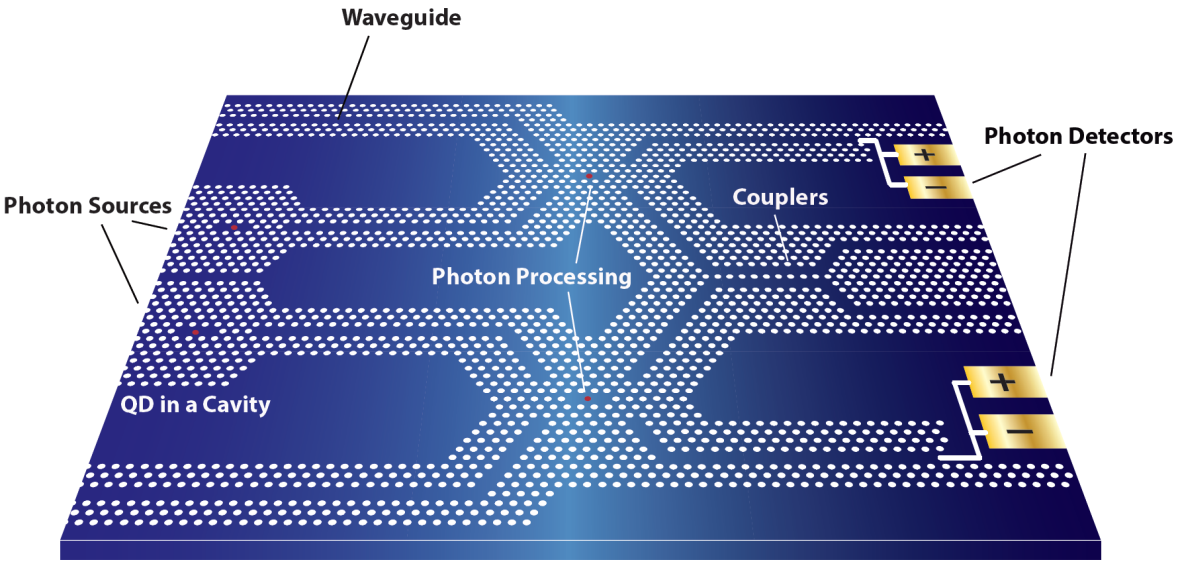

Figure 4.6: Schematic of future quantum network using photonic crystals.

The QD-cavity coupled system in the Purcell regime has demonstrated effective single photon generation [68, 69] which can provide quantum bits (qubits) for information processing. The strongly coupled QD-cavity system has possibilities to function as a high speed

and low power photon switch [10], modulator [70] and logic gate [71] by using their strong nonlinear responses. Waveguides and couplers can also be fabricated by photonic crystals, and on-chip photon detection can be achieved by implementing miniaturized superconducting nanowires [72]. One of the biggest obstacles to realize the photonic network using QDs was the random positioning of them during the growth process. However, recent progress in achieving site-controlled QDs has proved that site control can be a solution in the near future [16, 17, 19, 21, 23, 45, 52].

Chapter 5

Photonic Crystals Simulation and Measurement

In this chapter, we introduce a computational method that can characterize photonic crystal cavities by calculating resonant frequencies, quality (Q) factors and field patterns of cavity modes. The software used in this work is MEEP which is an open-source Linux-based free software [73, 74] for finite-difference time-domain calculation. The calculated resonant frequencies and cavity Qs by MEEP software are compared to the experimentally measured values at the end of this chapter. To experimentally measure the cavity modes, photoluminescence of quantum dot ensembles embedded in a cavity is measured and analyzed by polarization and spectrum.

5.1 Computational Method

5.1.1 Finite-Difference Time-Domain Calculation

Finite-difference time-domain (FDTD) is a computational method for modeling the propagation of electromagnetic waves in an arbitrary material by solving the Maxwell's equation

in discretized time and space. The idea originates from Kane Yee's algorithm [75] where the electric and magnetic field components are allocated to space grids and march in time steps for the space-time evolution. To illustrate this mechanism, let's consider a simple example in one dimension. First we write the Maxwell's equations in free space.

$$\frac{\partial \mathbf{E}}{\partial t} = \frac{1}{\varepsilon_0} \nabla \times \mathbf{H} \tag{5.1}$$

$$\frac{\partial \mathbf{H}}{\partial t} = -\frac{1}{\mu_0} \nabla \times \mathbf{E} \tag{5.2}$$

In a one-dimensional example, the above equations can be rewritten as

$$\frac{\partial E_x}{\partial t} = -\frac{1}{\varepsilon_0} \frac{\partial H_y}{\partial z} \tag{5.3}$$

$$\frac{\partial H_y}{\partial t} = -\frac{1}{\mu_0} \frac{\partial E_x}{\partial z} \tag{5.4}$$

which is a plane wave propagating in z direction.

Yee's algorithm uses a central difference approximation of the derivatives [Fig. 5.1] to numerically solve the Maxwell's equations.

$$\frac{E_x^{n+1/2}(k) - E_x^{n-1/2}(k)}{\Delta t} = -\frac{1}{\varepsilon_0} \frac{H_y^n(k+1/2) - H_y^n(k-1/2)}{\Delta z} \tag{5.5}$$

$$\frac{H_y^{n+1}(k+1/2) - H_y^n(k+1/2)}{\Delta t} = -\frac{1}{\mu_0} \frac{E_x^{n+1/2}(k+1) - E_x^{n+1/2}(k)}{\Delta z} \tag{5.6}$$

The Eq. 5.5 indicates that the change in the E-field in time is dependent on the change in the H-field across space (the curl). The result is the FDTD time-stepping where the field components are updated depending on the stored value of the E-field and the numerical curl

of the H-field distribution in space with increasing iteration, n. This scheme is also known as "leap-frog" algorithm [Fig. 5.2].

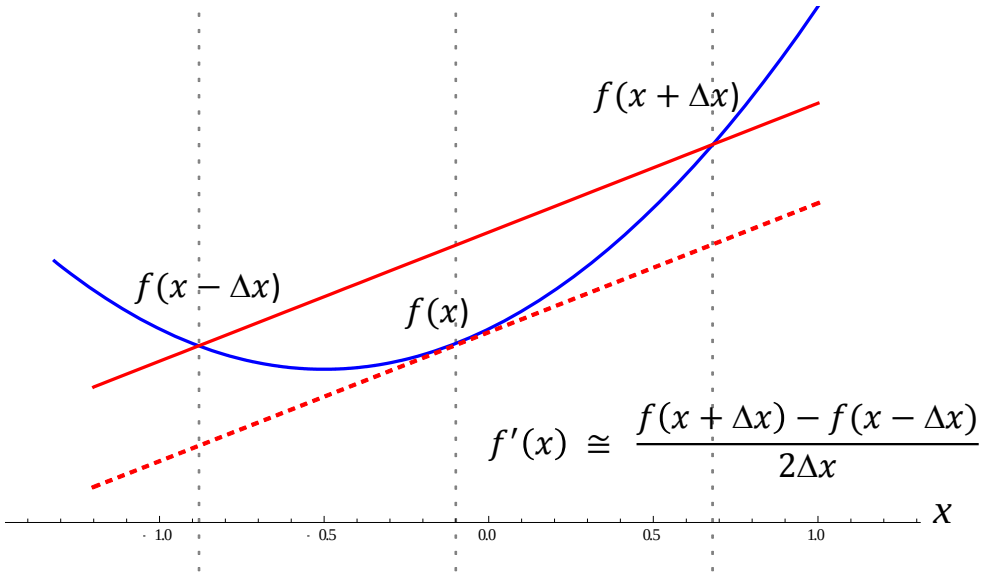

Figure 5.1: Central difference approximation.

To implement these equations in the numerical simulation, choosing the right values of Δt and Δz is important to reduce the computational time without sacrificing the temporal and spatial resolution. Generally Δz should be smaller than 1/10 of the wavelength to obtain adequate results. With this chosen cell size, the time step is also chosen considering the stability condition:

$$\Delta t \leq \frac{\Delta z}{c_o \sqrt{dim.}} \tag{5.7}$$

This means that a field component cannot travel more than one cell size in the time step Δt. A reasonable choice for Δt in three-dimensional is $\Delta z/2c_0$.

Also, to run a realistic simulation, it is important to consider boundary conditions. Since we cannot simulate the propagation in an infinite material, we need to terminate FDTD at a finite mesh without affecting the overall solution. The way to simulate open-end in

FDTD is called absorbing-boundary-conditions [76] and for MEEP it is implemented by perfectly-matched-layer which is a perfect absorber.

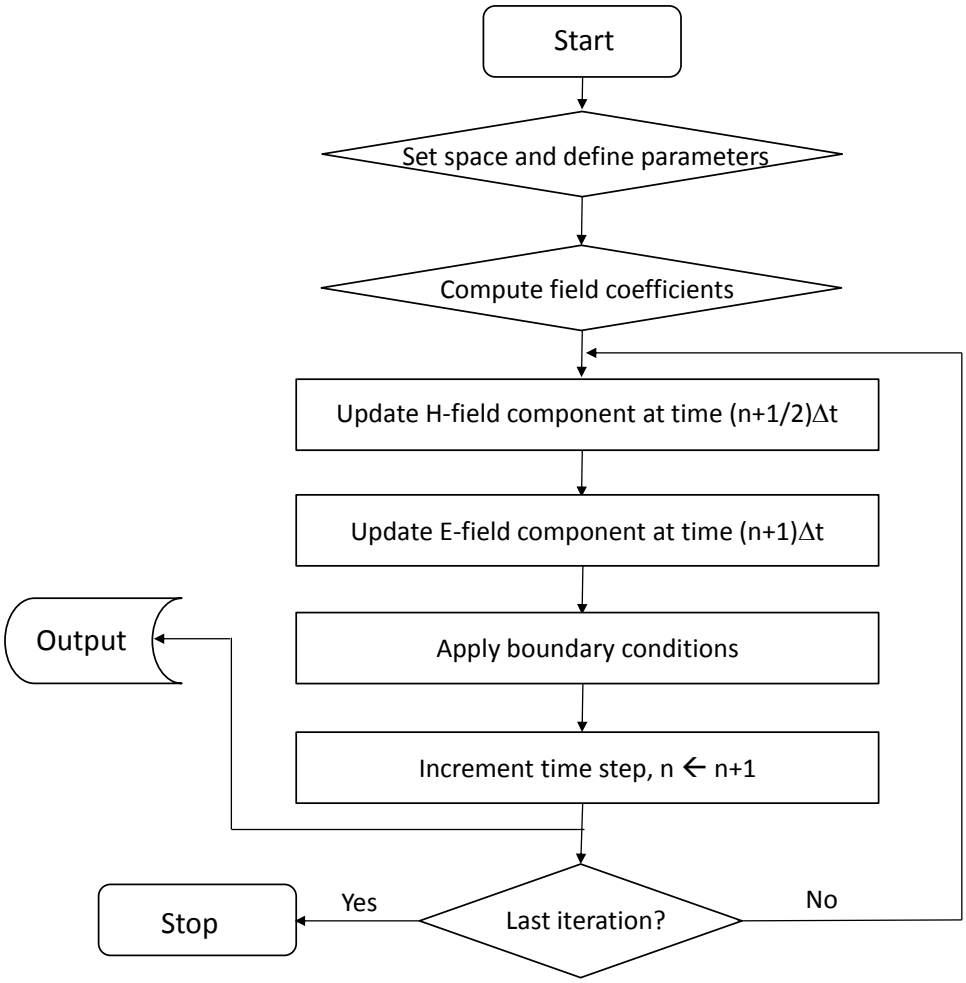

Figure 5.2: Leap-frog algorithm.

For a photonic crystal slab, FDTD methodology is the same to the free space case, but the spatial variation of the permittivity ε of a host material is added.

5.1.2 MEEP Simulation Results

The FDTD calculation is numerically performed using a simulation package called MEEP. With a 3D design of a photonic crystal cavity scripted in an input file, the light propagation

from a point source inside a cavity (placed in a non-symmetric arbitrary position) is simulated for a wide frequency range to find the cavity modes. Once the frequencies of the cavity modes are found, we run the simulation again at a resonant frequency to find the cavity mode field profile. All these simulations can be time-consuming if we use small cell sizes, but by exploiting structure symmetries the computation size can be incredibly reduced.

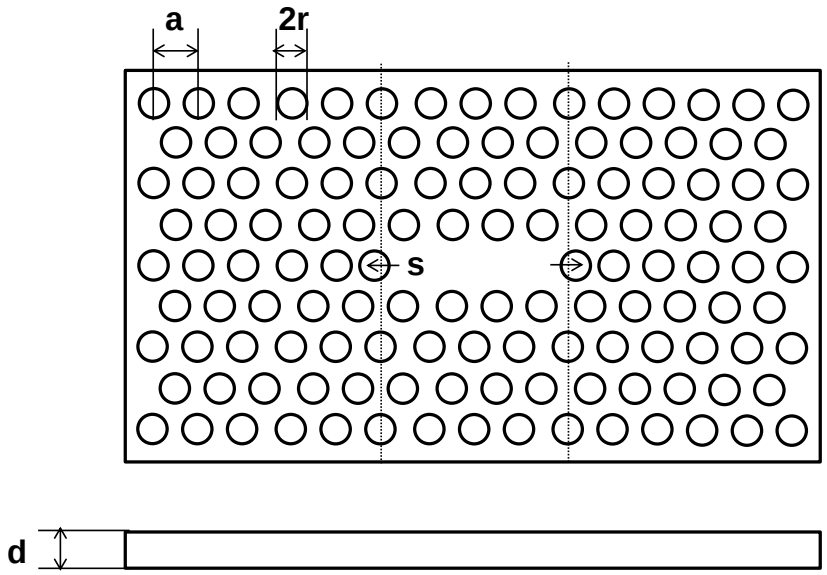

Figure 5.3: Hexagonal crystal $L3$ cavity design.

MEEP Parameter	a (lattice constant)	(e.g.) a = 284 nm
Hole radius (r)	0.31	88 nm
Edge hole shift (s)	0.15	43 nm
Slab thickness (d)	0.56	159 nm

Table 5.1: Parameters used for MEEP calculation of $L3$ GaAs (n = 3.59) cavity.

The input parameters to simulate a high Q cavity are shown in Table 5.1. The ratios between the lattice constant (a), air hole radius (r), edge shift (s), and slab thickness (d) are commonly accepted values for an optimized $L3$ photonic crystal cavity [77]. In particular, the implementation of the edge shift can significantly increase the cavity Q by forcing the gradual change of the field near the cavity edge which can lead to the reduction of the cavity loss [78]. With this edge shift, the theoretical cavity Q can be on the order of $\sim$ 10,000. In addition to the edge hole shift, Tim Saucer, et al. has found a cavity design with all-optimized cavity adjacent holes that can enhance the cavity Q by an order of magnitude [79].

For the actual cavity fabrication, the parameters in the right column of Table 5.1 are selected such that the cavity resonant wavelengths matches with the quantum dots that will be coupled to the cavities. When λ_{QD} = 950 nm, for example, by using the relation f = 0.29c/a = c/λ, we get the photonic crystal lattice constant a = 280 nm. From this lattice constant, we determine the cavity design including r, s, and d.

Using the parameters in Table 5.1, the calculated TE mode field profile is shown in Fig. 5.4. Depending on the field polarizations, we get different field profiles (b),(c). This well-localized field within the cavity can be seen in the simulation result at a time sufficiently long after the propagation of the initial point source starts. In addition to the field profile, we also obtained the cavity wavelength and Q-factor from simulation and converted them to the actual length using the lattice constant (a) for comparison to the experimental results [Fig. 5.7].

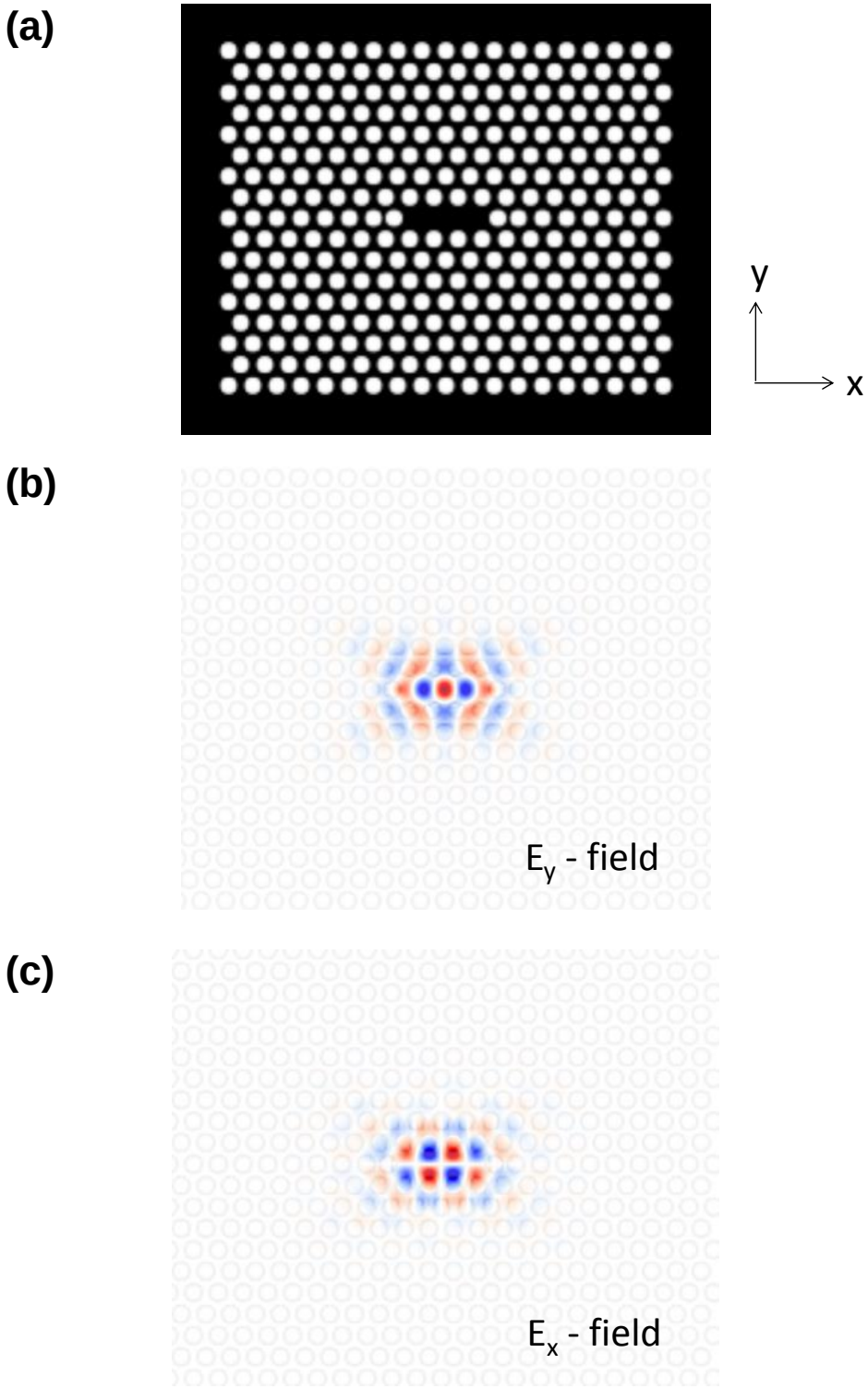

Figure 5.4: Field profile of *L*3 photonic crystal cavity (a) calculated by MEEP at different field polarizations (b)(c).

5.2 Cavity Q-factor measurement

The Q-factor of a cavity can be measured by transmission/reflection type measurement using a broadband white light source [80] or photoluminescence using broadband emitters within a cavity [7]. Here we show the Q-factor measurement using photoluminescence method with QDs as emitters.

5.2.1 Cavity Mode Probed by Quantum Dot Ensembles

The schematic of a QD sample we used for fabricating photonic crystal cavities is shown in the inset of Fig. 5.5. This sample was grown by Andrew Martin in the Millunchick group. In this sample, InAs QDs are embedded in the center of the GaAs slab which is 150 - 160 nm thick for cavity fabrication. This slab is grown on top of 1 μm thick AlGaAs layer which will be chemically etched so that the final cavities can be suspended in air.

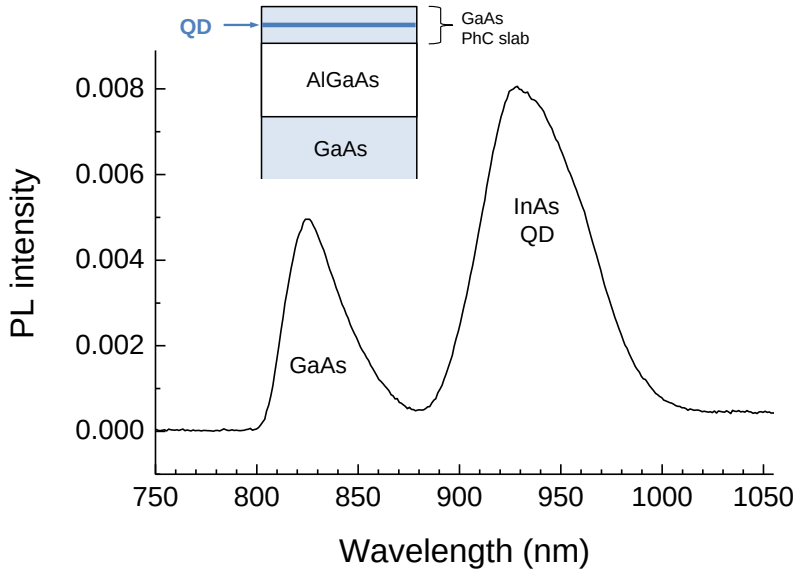

Figure 5.5: Photoluminescence of QDs in bulk GaAs substrate before fabricating photonic crystals. Spectrum was measured at T = 10 K with HeNe (λ = 633 nm) excitation power = 400 uW using InGaAs detector. Inset is the structure of the sample grown for cavity fabrication (GaAs substrate for PhC slab = 150 nm; QD = 2.3 ML; AlGaAs sacrificing layer = 1000 nm).

Fig. 5.5 shows the photoluminescence measured from these QDs. Strong PL from QD ensembles is detected at the wavelength centered around 930 nm without polarization dependency. With 2.3 ML of InAs thickness, typical QD PL is around 1000 nm, but we blue-shifted the QDs because we wanted the QD emission to be within the detection range of our Si CCD (350 - 950 nm). The blue-shift was done by annealing during growth process [81].

Then we fabricated photonic crystal cavities on this QD sample following the procedure in Appendix A. For the e-beam input design file, we used the target parameters a = {d/0.55, d/0.6, d/0.65}, s = 0.15a, r = {0.15a, 0.25a, 0.3a} with fixed d = 150 nm. The e-beam dose rate was varied which can further change the hole radius, r. Among 51 fabricated cavities, we were able to measure the cavity mode from 13 cavities that were successfully undercut. Note that r = 0.15a and 0.25a were too small for undercut and supporting a cavity mode.

We show the photoluminescence result from one of the cavities in Fig. 5.6. The emission from the cavity is measured in two different polarizations, 0 and 90 degrees (for orientations, see Fig. 6.1.) While we did not observe polarization dependency in bulk QD emission, we see sharp emission features with QDs in a cavity only at a certain polarization. This is because of the Purcell enhanced emission from QDs that are resonant to cavity modes. These cavity modes exist at both 0 and 90 degrees but at different wavelengths (see Fig. 5.4) [82].

From cavity-enhanced QD emissions, we can calculate the Q-factor of a cavity.

$$Q = \frac{f_0}{\Delta f} \tag{5.8}$$

Using the above relation, we obtain Q = 110 and 921 for cavity mode field direction in 0 and 90 degrees, respectively.

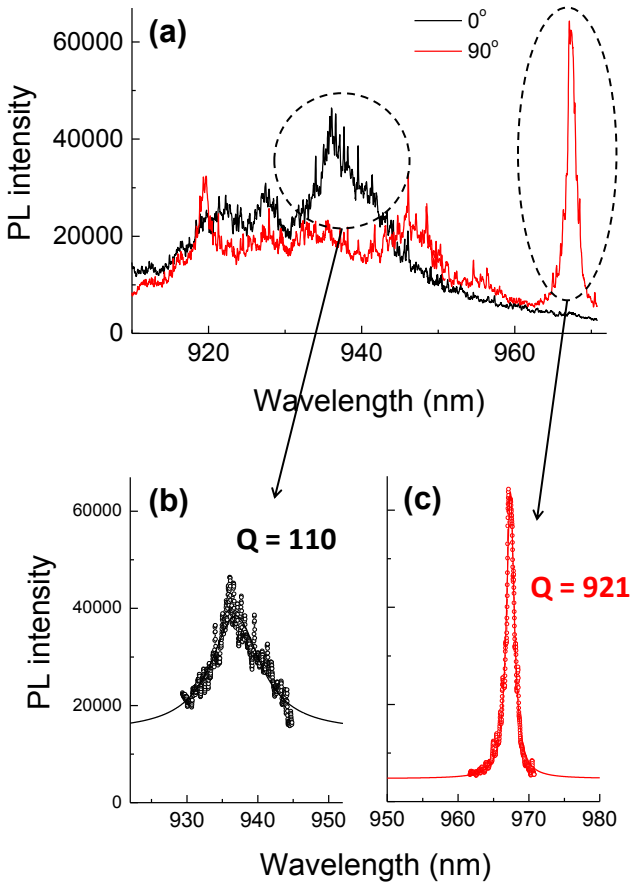

Figure 5.6: Photoluminescence of QDs in a photonic crystal cavity at 10 K. QD emissions are enhanced for those that are resonant to cavity modes. (b), (c) Q-factor measurement. Cavity mode can exist in different polarizations.

5.2.2 Comparing Measurements to MEEP Results

We summarize the measured cavity mode wavelengths and cavity Qs in Fig. 5.7. The lattice constant and hole radius are measured from the actual fabricated cavities by SEM. MEEP results are plotted together for comparison. The general trends of wavelengths and cavity Qs are similar between experiments and calculations. However, there is about 10 % discrepancy which could have originated from an inaccurate GaAs refractive index or cavity geometry used for the calculation. In addition, MEEP predicted that a very high Q can be achieved

for cavity with a = 283 nm and r = 0.31a, which was not observed in our data. This may be due to the imperfect undercut, not achieving the optimum cavity dimensions and sidewall angle, and debris left on the cavity which can be further improved by optimizing the etching process. We expect that the fabricated cavity Q can be increased by at least an order of magnitude by further optimizing the cavity design and fabrication process. Other groups have reported cavity Q's $> 10^4$ for similar GaAs L3 cavities [9, 77] and $> 10^6$ in silicon heterostructure [83], waveguide-type [84] and L3 [85] cavities.

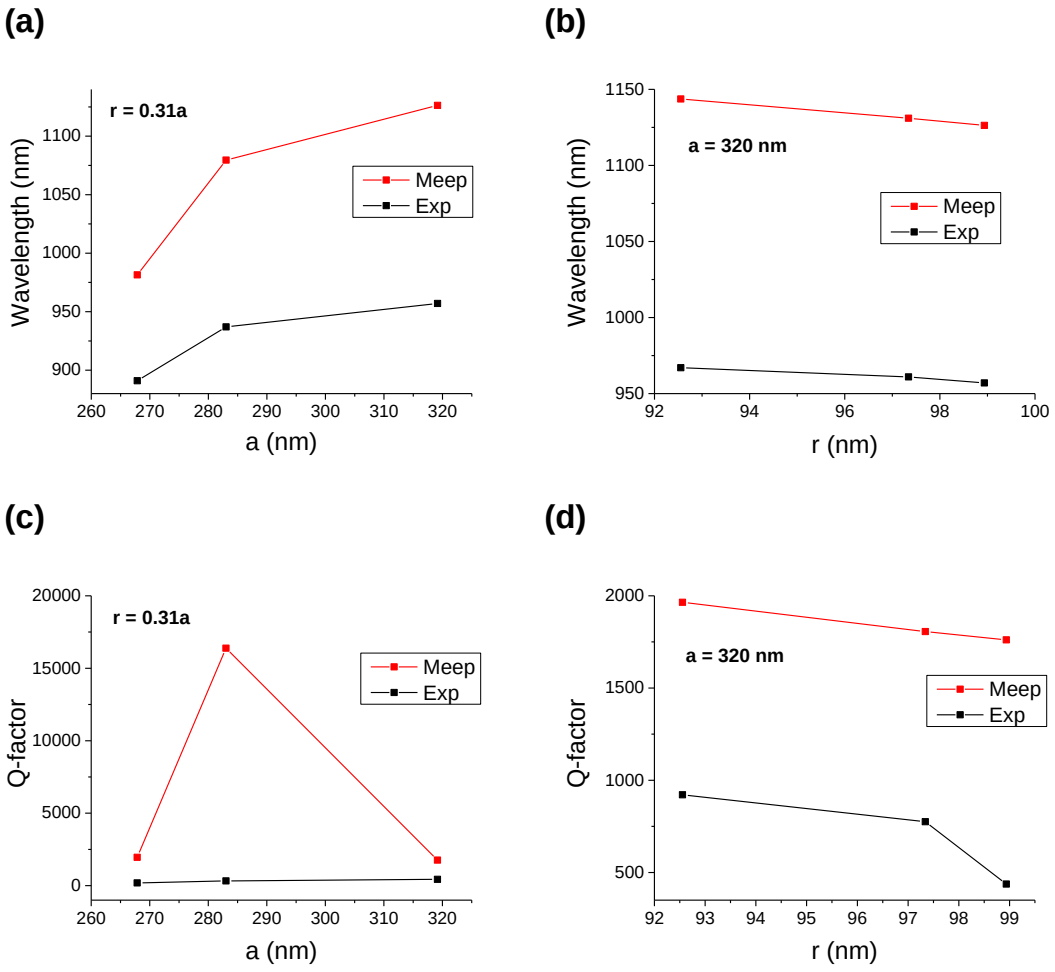

Figure 5.7: Cavity mode wavelength and Q-factor as functions of crystal lattice constant (a) and hole radius (r) obtained from experiment and MEEP calculation.

Chapter 6

Nonlinear Dynamics of Quantum Dots in a Photonic Cavity

6.1 Motivation

In the field of cavity quantum electrodynamics (QED), tailoring the optical environment of a quantum emitter can lead to the modification of spontaneous emission as first discovered by Purcell [65] and demonstrated in atoms [64] and solid-state systems [7, 86, 87]. The ability to modify the temporal and spectral features of quantum emitters using cavity QED is expected to greatly enhance the performance of optoelectronic devices such as quantum gates and micro-lasers. It has been recognized that for these applications utilizing the nonlinear optical response of cavity-coupled quantum emitters is advantageous [8, 88, 89]. For example, recent experiments have shown the ultrafast switching of two weak laser pulses enabled by the nonlinear response of a strongly coupled solid-state system [10, 90]. Earlier measurements in the weak coupling regime have also revealed complex nonlinear coupling dynamics [91].

Despite the importance of nonlinearity in cavity QED for both strong and weak coupling regimes, the effects of nonlinearity in modifying the temporal dynamics and quantum yield

of coupled systems are not fully understood. In this work, we use luminescence intensity autocorrelation (LIA) to experimentally and theoretically investigate the dynamics of single emitters whose emission are enhanced by the Purcell effect, at various power regimes. This approach enables the direct visualization of the nonlinear emission as a function of time under constant incident power.

LIA is a time-resolved optical measurement that monitors the emission as a function of the delay time between two optical excitation pulses. Therefore both the power-dependent and time-resolved response of the excitation and emission can be simultaneously studied, with the temporal resolution limited only by the duration of the laser pulse. For LIA, the radiative lifetime of an emitter is measured through the nonlinear response of the time-averaged emission intensity, which is inherently different from time-resolved photo-detection methods using streak cameras [92] or photon correlation measurements [93].

Here we present a study on the nonlinear dynamics of single quantum dots (QDs) coupled to photonic crystal (PhC) cavities. The Purcell effect by the cavity is demonstrated by performing LIA on QDs both coupled and uncoupled to a cavity. The enhanced spontaneous emission of the cavity-coupled QDs enables a strong LIA signal which evolves when varying the incident power over a wide range. We also observe distinct differences between exciton and biexciton LIA, demonstrating the potential of LIA as a tool to identify the QD transitions.

The results described in this chapter have been published in Ref. [94].

6.2 Sample Preparation

For sample fabrication, 2.3 monolayers of InAs were deposited for QD nucleation and subsequently annealed at the growth temperature in order to blue-shift the emission wavelength [81]. Under these growth conditions, QDs nucleate with a density of $500/\mu m^2$ as verified by

atomic force microscopy of an uncapped sample. For PhC fabrication, QDs are grown in the middle of a 150 nm GaAs layer which forms the membrane of the PhC. The final $L3$ cavity looks similar to the SEM image in Fig. 6.1.

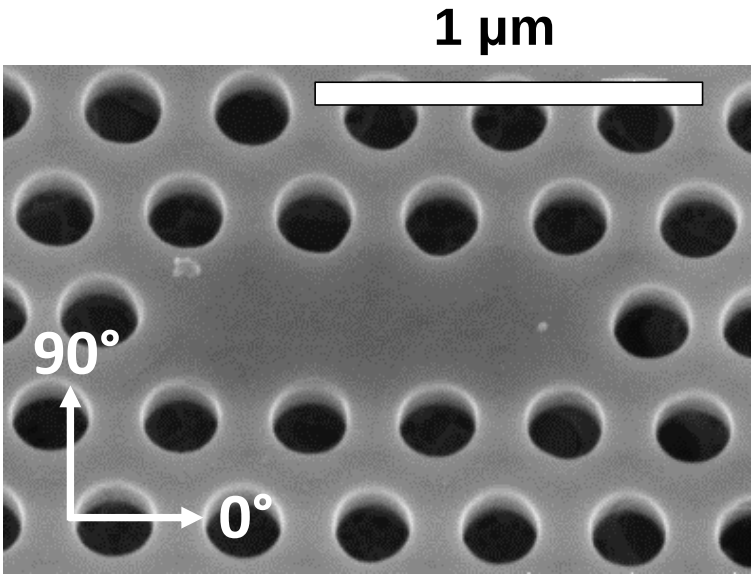

Figure 6.1: Scanning Electron Microscopy image of the fabricated $L3$ cavity. This image is tilted by 20°. The arrows show the polarization of the collected PL. Reprinted figure with permission from [94]. Copyright (2013) by the American Physical Society.

6.3 Time-resolved Pump-pump Set-up

The set-up for optical measurements is shown in Fig. 6.2. The optical characterization of the QDs coupled to the PhC cavity is carried out using a HeNe laser. For the time-resolved experiment, pulses from a modelocked picosecond Ti:S laser (76 MHz repetition rate) tuned to a center wavelength of 780 nm with controlled time delay are used as the excitation source. An objective lens with numerical aperture NA = 0.7 and a fast-steering mirror controlling the beam path going to the sample are used to focus the beam on the cavity with 5 μm

beam diameter. The emitted light from the sample is collected by the same objective lens and spatially resolved by a translational confocal microscopy configuration with a pinhole used as an aperture to selectively collect emission from QDs coupled to the cavity [52]. The collected light is recorded by a CCD detector with 1 s exposure time. The sample temperature was set to 10 K by a Helium-flow cryostat for all measurements.

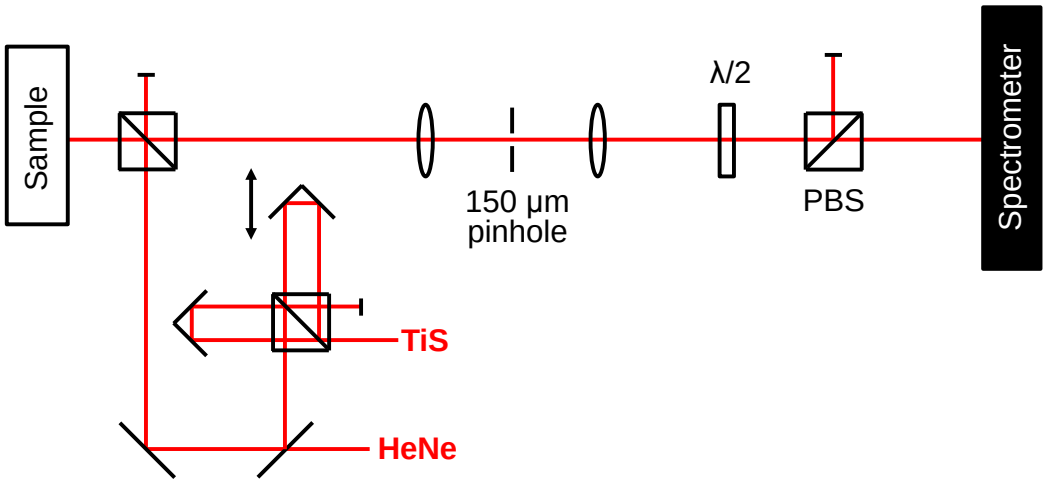

Figure 6.2: Luminescence intensity autocorrelation set-up. Ti:S provides laser pulses for pump-pump time-resolved autocorrelation experiment, whereas HeNe provides CW excitation for the cavity mode spectral characterization. Reprinted figure with permission from [94]. Copyright (2013) by the American Physical Society.

6.4 Experimental Results

6.4.1 Purcell enhanced emission of cavity-coupled QDs

The coupling between the PhC cavity and QDs are studied by polarization-dependent micro-photoluminescence (PL) measurements as shown in Fig. **??**. PL from QDs with emission wavelength well within the cavity mode are Purcell enhanced only when the PL polarization is parallel to the cavity mode field direction which is at 0° in this cavity [74]. From the

Lorentzian fit of the Purcell enhanced PL at a laser power = 190 μW, the calculated cavity Q = 190 which corresponds to the cavity loss rate κ = 5500 GHz. At a lower laser power = 0.28 μW, a smaller number of Purcell enhanced QD emissions are observed. For both powers, the 90° polarized light emission is suppressed due to the polarization mismatch to the cavity mode [7].

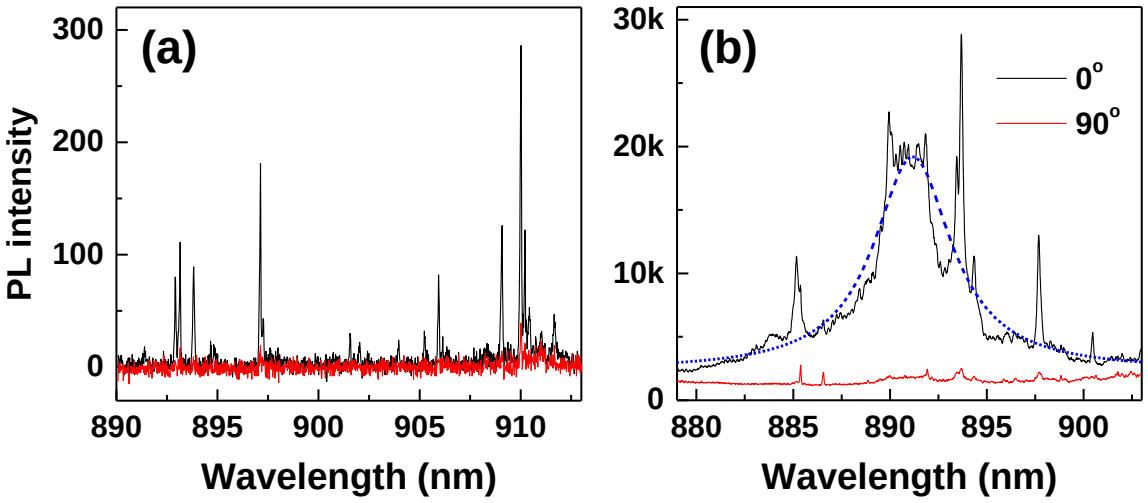

Figure 6.3: Purcell enhancement of PL from QDs embedded in a PhC cavity. The HeNe laser polarization was set to 45° relative to the cavity and the PL was collected at either 0 or 90° (see Fig. 6.1) by using a half-wave plate ($\lambda/2$) and a polarizing beam splitter (PBS) as shown in Fig. 6.2. (a) PL spectra measured when laser power = 0.28 μW. (b) PL spectra measured at a laser power = 190 μW. Blue dashed line is the Lorentzian fit. Reprinted figure with permission from [94]. Copyright (2013) by the American Physical Society.

6.4.2 Nonlinear Luminescence Autocorrelation

In order to evaluate the Purcell enhancement by the cavity, we directly measure the lifetime of the QDs using LIA. For the time-resolved experiment, two Ti:S pulses arrive at the sample with a relative time delay τ_d which is controlled by a mechanical delay line on one arm of

the laser path [Fig. 6.2]. To verify that the position of the delay line has minimal effect on the optical alignment, we first measured the PL when scanning the delay line and with the beam going to the other (fixed) path blocked. With the blocked fixed line, the 2D plot of the PL from three QDs coupled to the cavity while scanning the delay line is shown in Fig. 6.4(a). For every measurement, the variation in PL intensity for a delay line scan with the fixed path blocked was maintained to be below 5 %.

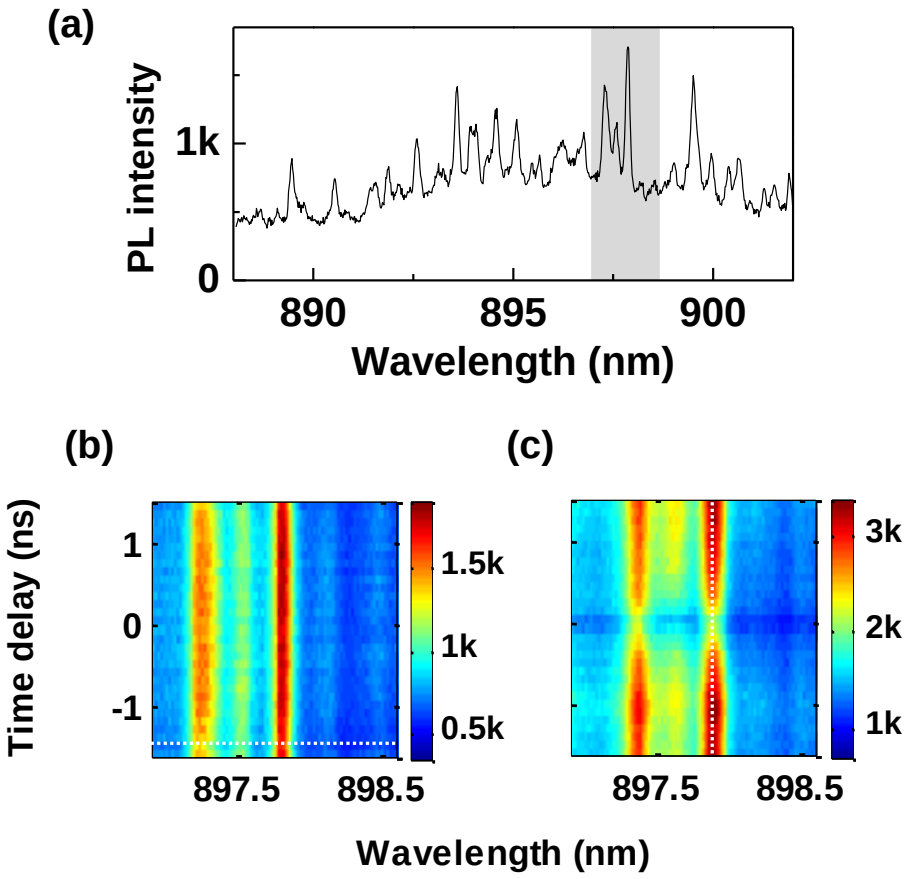

Figure 6.4: Luminescence intensity autocorrelation data. (b) The measured 2D plot shows the PL intensity of three QDs while varying the delay line position with the fixed line blocked. The measured spectrum at a delay line position (horizontal white line) is shown in the shaded area of (a). (c) The PL intensity with both arms unblocked exhibits a dependence on time delay. Reprinted figure with permission from [94]. Copyright (2013) by the American Physical Society.

We then performed the time-resolved experiment with pulses from both the delay line

and fixed arms on the same QDs [Fig. 6.4(b)]. For a long delay between pulses (> 1.5 ns), the PL intensity becomes about twice that of a single pulse, but when the two pulses are overlapped around zero time delay, the PL decreases. Such delay time dependence is observed in several QDs for the selected laser power ($= 36$ μW). The appearance of the dip at this laser power is related to the radiative recombination time (τ) of the QD. The origin of the dip will be examined in more detail with the simulation described below. Fitting the data to the exponential decay function $I = I_0 - I_1 \exp(-\tau_d/\tau)$, for the QD with $\lambda = 897.7$ nm, we found $\tau = 0.5$ ns [Fig. 6.5, black filled circles]. The autocorrelation function of the laser pulse is also plotted for reference.

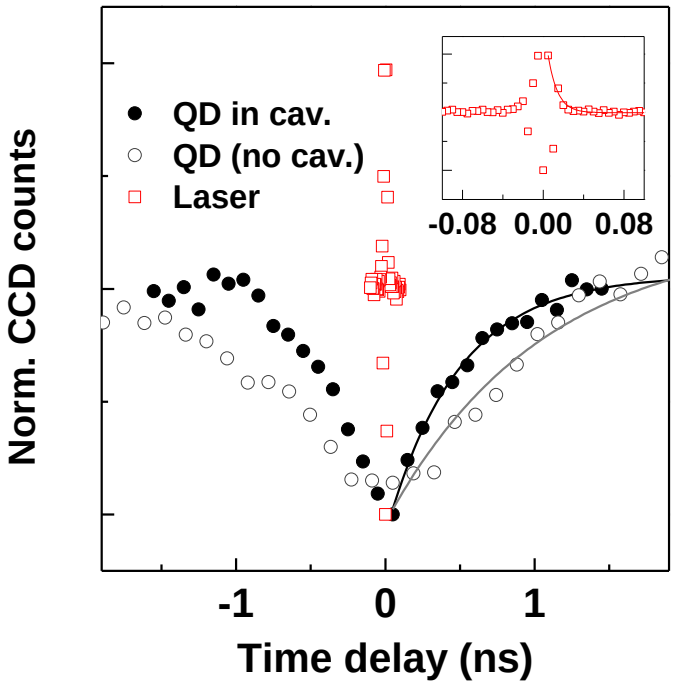

Figure 6.5: The black filled circles are measured from a cavity-enhanced QD and correspond to the vertical white line in Fig. 6.4(c). The grey open circles are from a QD that is not in a cavity. The inset shows the extended view of the laser autocorrelation (red open squares). For comparison of time-resolved data between QDs and laser autocorrelation, the detector CCD counts at large time delays are normalized. The time-resolved data of both QDs and the laser are fitted to the exponential decay function. Reprinted figure with permission from [94]. Copyright (2013) by the American Physical Society.

To compare the lifetime of the Purcell enhanced QD to a QD without a cavity, we also measured LIA for a single QD with a similar emission wavelength in a different sample which has no cavity [Fig. 6.5, grey open circles], and the measured $\tau = 1$ ns, similar to lifetimes of previously reported InAs QDs. Therefore the extracted Purcell factor F = 2 for this selected QD. The largest F we observed in this cavity is 4, corresponding to a measured $\tau = 0.25$ ns. The variation of the measured Purcell factor from QDs is due to the different spatial and spectral match to the cavity mode [7]. If there is no spatial and spectral mismatch, the estimation of the Purcell factor with the given Q and V_{mode} is about 20.

6.4.3 Exciton Nonlinearity

We studied LIA in more detail by varying the laser power. Fig. 6.6(a) shows the experimentally measured PL intensity of a QD exciton as a function of time delay where the laser power increases from 0.1 to 71.9 μW. The laser power where the dip starts to appear is near where the QD emission saturates. This indicates that the evolution of LIA by varying the laser power results from the QD nonlinearity. Such QD nonlinearity is due to an atom-like quantized energy state of a single QD. It should be noted that this clear relation between the QD power dependence and LIA was not observed for an ensemble of QDs [95].

To understand the origin of the dip at high laser power where the QD emission saturates, let us consider the two cases where (i) $\tau_d = 0$ and (ii) $\tau_d >> \tau$. We are interested in a laser power where a single laser pulse can completely fill the QD exciton state. At $\tau_d = 0$, two laser pulses arrive at the QD simultaneously but they can fill the QD exciton state once. However, when $\tau_d >> \tau$, the first and the second pulse can each independently fill the QD since the exciton excited by the first pulse has enough time to relax before the second pulse arrives. Therefore we expect that the number of excitons generated when $\tau_d = 0$ to be half of when $\tau_d >> \tau$. In the experimental data, the ratios PL($\tau_d = 0$) / PL($\tau_d >> \tau$) of the 3 highest powers are $\{0.68, 0.64, 0.63\}$ for P = $\{7.3, 29.7, 71.9\}$ μW. As the laser power increases, the

ratio approaches the expected value of 0.5. We consider that the experimentally observed ratio is higher than 0.5 due to imperfect alignment and a finite time step $\Delta\tau_d$ (= 0.13 ns).

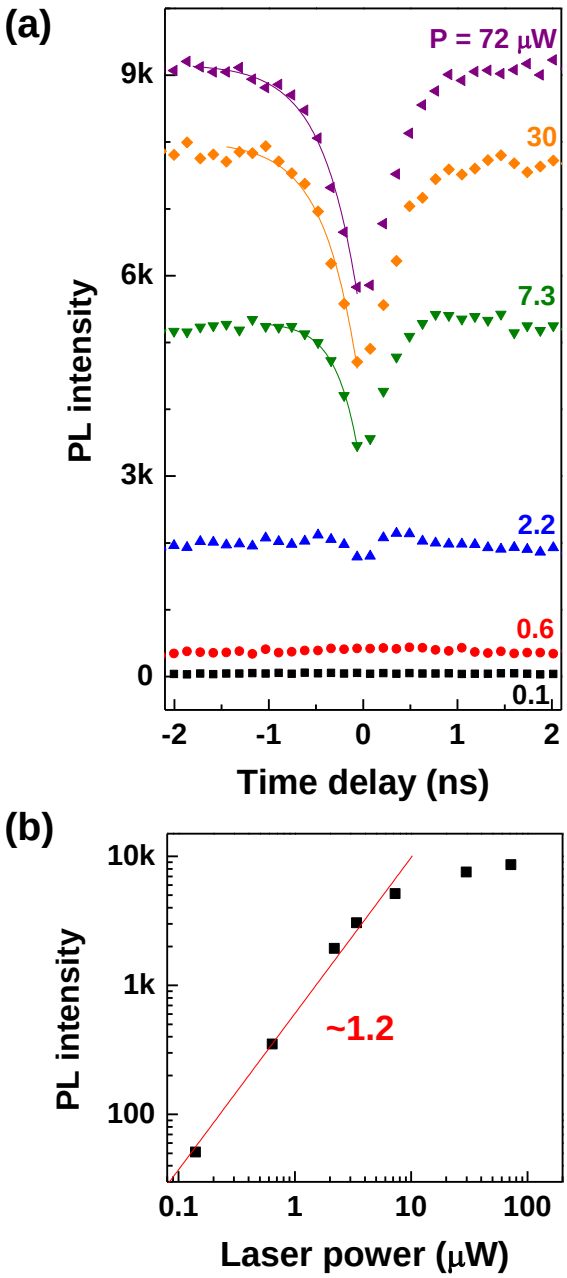

Figure 6.6: Power-dependent LIA of an exciton. (b) The linear power-dependence before the PL saturation shows that the peak is from an exciton. (a) From bottom to top, laser power increases. At the laser power where the QD nonlinearity appears, the dip starts to evolve in the time-resolved LIA. Reprinted figure with permission from [94]. Copyright (2013) by the American Physical Society.

The lifetime τ obtained from the 3 highest powers are $\{0.24, 0.38, 0.39\}$ ns for P = $\{7.3, 29.7, 71.9\}$ μW. Here the QD lifetime is increasing with laser power and saturating at some point. Note that the increase and saturation of τ with power was also observed on several QDs in a different cavity [Fig. 6.7]. The increase of τ, together with the decrease of the ratio PL($\tau_d = 0$) / PL($\tau_d >> \tau$), at the intermediate power range is the result of the partial state filling ($< 100\%$) of the exciton state in the QD by the first pulse.

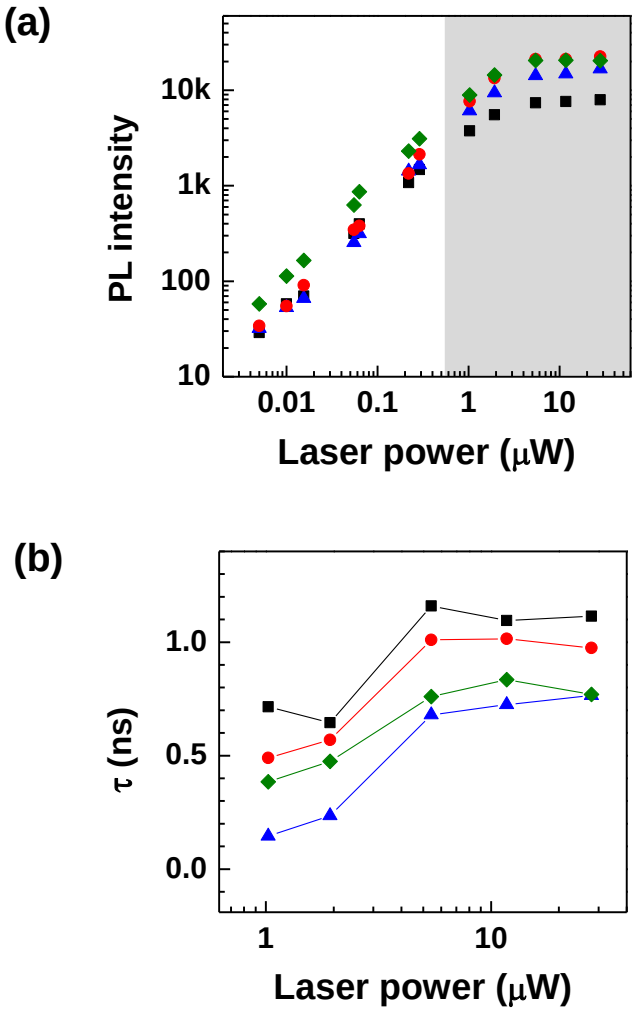

Figure 6.7: (a) PL intensity and (b) extracted exciton lifetime of four different QDs in a different cavity (Q = 680) as a function of laser power. Lifetimes are measured for the nonlinear power range (shaded area). Reprinted figure with permission from [94]. Copyright (2013) by the American Physical Society.

6.4.4 Biexciton Nonlinearity

In this section, we show the experimental result of QD biexciton emission in Fig. 6.8. Due to the superlinear power dependence in the low power regime, the PL intensity at zero delay time is higher than the PL at large time delays.

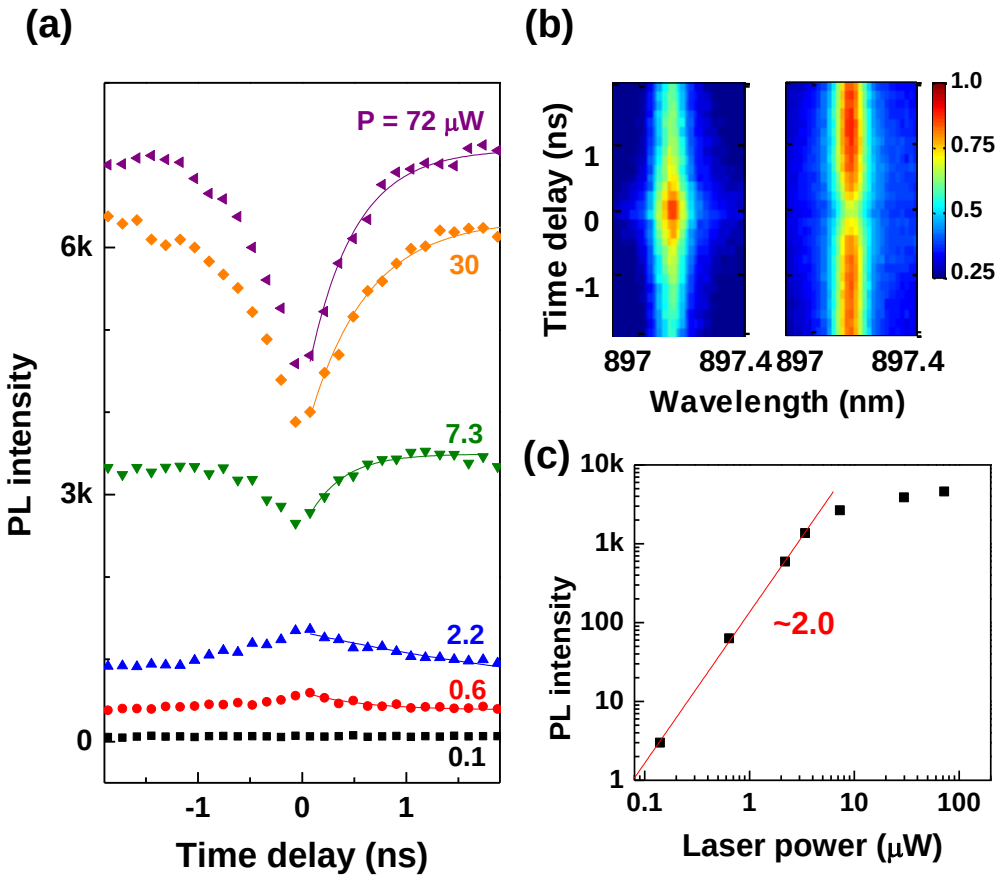

Figure 6.8: Power-dependent LIA of a biexciton. (a) Unlike the exciton, biexciton emission shows a rise at low laser powers. This is consistent with the superlinear power dependence of the biexciton emission (c). τ from an exponential fit from bottom to top are 0.6, 3.5, 0.33, 0.56, 0.44 ns (lowest laser power excluded). (b) The change from rise to dip is more apparent in the 2D plot (Left: P = 2.2 μW, Right: P = 7.3 μW). The color scales of both plots are normalized. Reprinted figure with permission from [94]. Copyright (2013) by the American Physical Society.

Such a rise at low power can be understood by the formation of a biexciton through the combination of two excitons, one from each of the first and the second laser pulse, which is possible only when the two pulses arrive within the lifetime of the exciton. Therefore the fitted τ at low laser power is related to the recombination time of both the exciton and biexciton [96]. At higher laser power, the sublinear power dependence results in a dip in the time-resolved data, similar to what we observe for exciton emission. At the lowest laser power, no features are observed due to the reduced probability of creating a biexciton. In our sample, due to the high density of QDs, the corresponding exciton peak of this biexciton was hard to identify. By isolating the emission from a single QD, direct comparison between the QD exciton and biexciton lifetime will be possible.

6.5 Quantum Optical Simulation

In order to model the experimental data, we have conducted a simulation using the quantum optics toolbox [97]. In the simulation, we first constructed the Jaynes-Cummings Hamiltonian that takes into account the interaction between the two-level system and the cavity photon mode. The QD transition and cavity mode are assumed to be degenerate, similar to the selected experimental data. The pulsed laser is introduced as two Gaussian functions (width = 10 ps) with a time delay. Here the energy of the laser is assumed to be resonant with the QD and the cavity, which is reasonable because any coherent effects due to the laser in the simulation cannot last longer than the pulse width (10 ps) which is much shorter than τ and the timescale of the dynamics that we are interested in. The dissipation factors are phenomenologically included in the Lindblad form for all calculations: $\kappa = 5500$ GHz, $\gamma = 1$ GHz, $\gamma_d = 40$ GHz. Here κ, γ, and γ_d are the cavity loss rate, QD transition rate, and the QD dephasing rate, respectively. κ and γ_d are from the measured cavity and QD emission width and γ is from the measured τ of the cavity-uncoupled QD. The dot-cavity

coupling strength g is obtained by finding a best fit and the resultant g = 42 GHz. From these parameters, the calculated critical photon number $n_0 = 0.01$ which is well below one. The critical photon number is a measure of the number of photons required in the cavity mode in order to saturate the QD [98]. Therefore any photon number N above n_0 could be used to include the power nonlinearity in the simulation. In our calculation, using photon number $N = 1$ to 4 showed similar results. The single pulse amplitude E was varied to incorporate the varying laser power of the two pulses ($2E^2$). An alternative to this quantum optical simulation has also been reported which solves the nonlinear semiclassical model [99].

In our simulation, the average QD exciton state population <P(X)> was calculated for each E while varying the time delay between the two pulses. We find excellent similarity between the experimental data and the simulation [Fig. 6.9]. In addition, the dip in the simulation starts to appear at the power where <P(X)> saturates which is consistent with the experimental data. Using a single set of physical parameters, the lifetime τ of the simulation in the nonlinear regime is 0.38 ns for all E. The peak around zero time delay is the result of resonant excitation that could not be washed out in the simulation within the pulse overlap ($\tau_d < 20$ ps).

Parameter	Symbol	Value (GHz)	Source
Cavity decay	κ	5500	Cavity Q measurement
Bulk QD decay	γ	1	QD LIA measurement
QD pure dephasing	γ_d	40	QD spectral width
Coupling rate	g	42	Fitting

Table 6.1: Coupling and dissipation parameters used for quantum optical simulation.

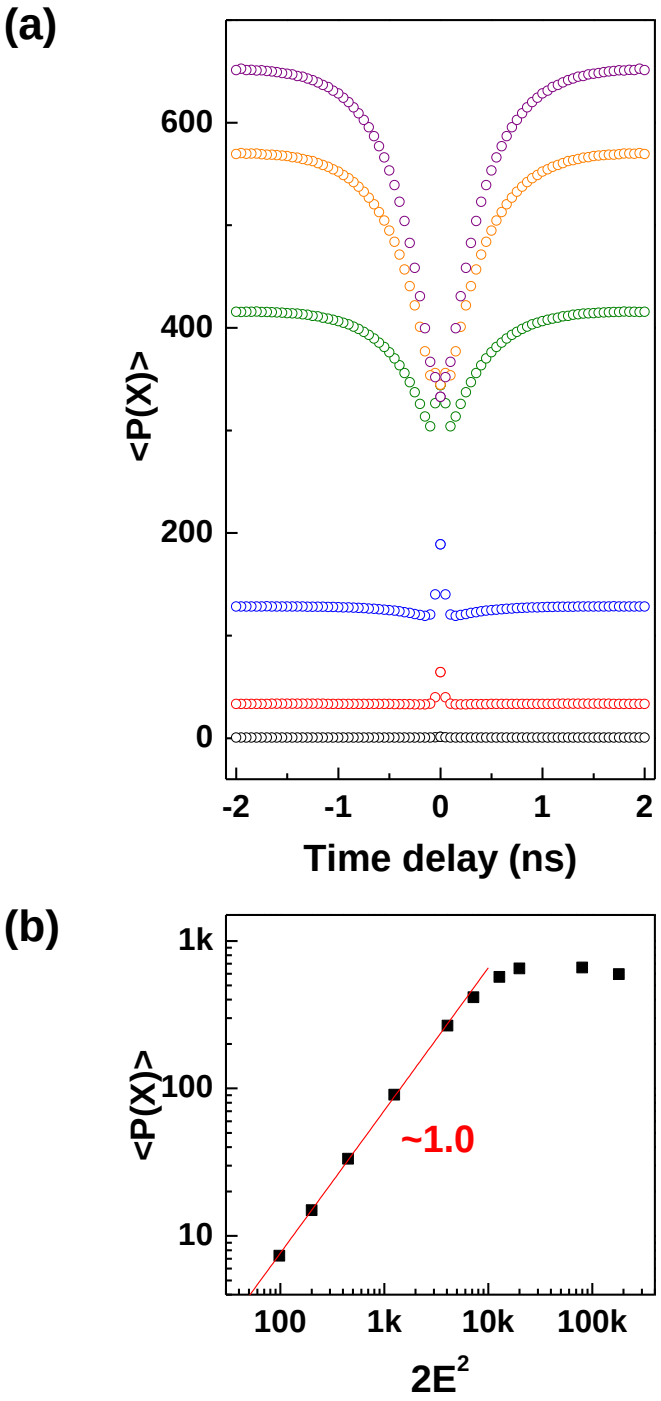

Figure 6.9: Quantum optical simulation result of exciton luminescence intensity autocorrelation. This result is very similar to the experimental data in Fig. 6.6. Reprinted figure with permission from [94]. Copyright (2013) by the American Physical Society.

6.6 Conclusions

In conclusion, the nonlinear dynamics of a dot-cavity coupled system is studied by LIA, which is a power-dependent and time-resolved measurement method using two time-delayed degenerate laser pulses. Modeling the excitonic LIA using a quantum optical simulation, we found physical parameters governing the coupling (g) and emission dynamics (κ, γ) for a cavity-coupled QD in the Purcell regime. The LIA signal of the Purcell enhanced QD is negative (dip) for laser powers above the dot saturation point, which is qualitatively the same to the QD outside the cavity except that the dip is narrower due to the shorter lifetime. We expect that positive or even oscillating excitonic LIA can be observed by increasing Q to the strong coupling [10, 90] or lasing regime [91]. This method can be applied to study the nonlinear emission dynamics of various types of quantum structures for the next generation of quantum lasers and quantum information processing.

Chapter 7

Summary and Future Works

In this thesis, I have investigated methods to spatially and temporally control InAs quantum dots for on-chip integration. Site-controlled quantum dots patterned by a focused-ion-beam are examined optically using scanning micro-photoluminescence. I found that the line-width broadening of site-controlled dots can be improved by vertically separating quantum dots from the seed dots through stacking multi-layers of dots. Quantum dots in the upper layers are nucleated at laterally shifted positions from the seed dots due to the mounds formed at focused-ion-beam patterned sites, which can be improved by optimizing the growth conditions including the spacer layer thickness and focused-ion-beam dwell time [44, 46]. The temporal control of quantum dot emission was achieved by coupling dots to photonic crystal cavities. Purcell enhancement of dot emission rate is demonstrated by luminescence intensity autocorrelation. In addition, nonlinear emission dynamics of quantum dot exciton and biexciton are explained with the excited-state-filling mechanism. Quantum optical simulation of exciton has further supported our data interpretation and enabled the extraction of dot-cavity coupling strengths. I expect that the luminescence autocorrelation experiment and simulation tool can be used to understand other nonlinear phenomena in quantum two-level systems [91, 100].

Below I suggest future works related to the site-controlled quantum dots and photonic crystal cavities.

- Deterministic coupling between focused-ion-beam-induced quantum dots and photonic crystal cavities. This will require fabricating two or three-layer quantum dot samples and accurate reading of quantum dot positions, fabrication of alignment markers [18] and positioning of the markers during e-beam lithography.

- Luminescence autocorrelation experiment of a quantum dot strongly coupled to a photonic crystal cavity. To achieve strong coupling, it is necessary to increase the Q of the cavities through fabrication improvement or design optimization [79, 85].

- Coupling two or more quantum dots within a cavity or in multiple cavities through mediating photons. Spatial control of quantum dots using a focused-ion beam and deterministic integration to photonic crystal cavities are expected to greatly increase the chance to achieve coupling between multiple quantum dots.

Furthermore, driving quantum dots in photonic crystals by electrical excitation [101] will enable single photon generation and quantum gate operation without optical fields which will be beneficial for realizing a lab-on-a-chip using quantum circuits in combination with on-chip single photon detectors [72].

Appendix A

Photonic Crystal Fabrication

Here we summarize the steps required to fabricate photonic crystals on a InAs/GaAs quantum dot sample (see the inset of Fig. 5.5 for the sample structure). All processes are carried out at the Lurie Nanofabrication Facility.

A.1 Sample Preparation

- Prepare sample with a clean surface by checking with an optical microscope.
- The size of the sample should be bigger than the minimum size that the resist spinner can hold by vacuum suction.
- Dip the sample into acetone for 60 s and isopropanol (IPA) for 60 s without an interval and dry with nitrogen blowing. Repeat if necessary.

A.2 E-beam Lithography

- Prepare the resist PMMA A4 (polymethyl methacrylate diluted in 4% anisole).

- Spin coat the resist PMMA A4 on the sample at 1000 RPM for 45 s (ramp 500 RPM/sec). Target resist thickness = 400 nm.

  (If using PMMA A6, spin at 3000 RPM for 60 s (ramp 1500 RPM/s).)

- Soft bake at 180°C for 2 mins.

- Expose the sample to e-beam using either Raith 150 or JEOL 6300. JEOL 6300 in 5th lens mode can achieve resolution down to a few nanometers.

- Develop the exposed sample in 25 % MIBK (methyl isobutyl ketone) for 50 s and rinse MIBK with IPA for 60 s. Dry IPA with a gentle blow of nitrogen.

- Bake at 80°C for 10 s.

- Check if the photonic crystal patterns are transferred to PMMA by using either a microscope or SEM [Fig. A.2]. Note that imaging PMMA with SEM can harden PMMA which can affect etching.

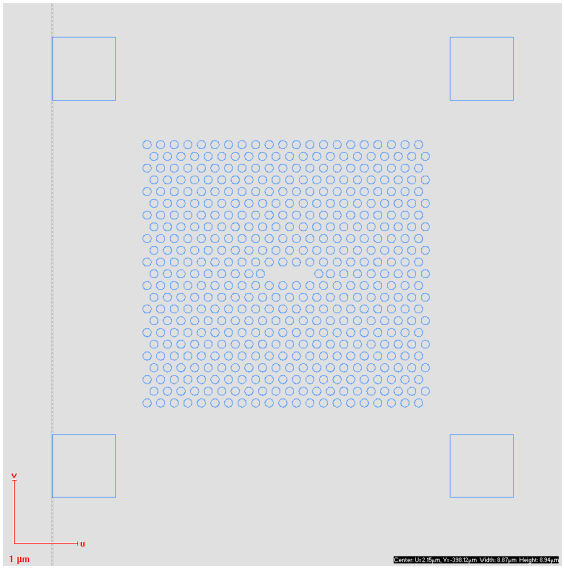

Figure A.1: Image generated by a photonic crystal design file for e-beam Raith 150. Four squares in corners are designed to help undercutting, which are optional.

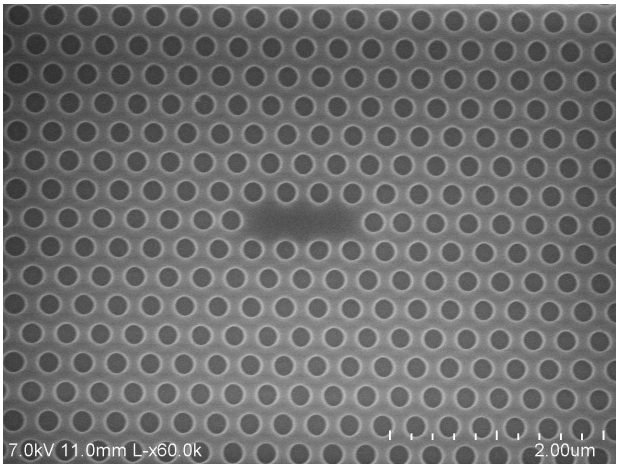

Figure A.2: SEM image of a PMMA mask fabricated by e-beam JEOL 6300.

A.3 Dry Etching

- Etch the sample using the recipe below by Oxford PlasmaLab 100.

Temperature	5 °C
Pressure	3 mTorr
Cl_2	2 sccm
Ar	10 sccm
BCl_3	8 sccm
RF power	47 W
ICP	200 W
Time	90 s

Table A.1: Etch recipe using Oxford PlasmaLab 100.

- Note that stabilizing the chamber with the same recipe for 30 - 60 mins. before etching the sample helps to increase the repeatability.
- It may be necessary to update the etch recipe after the chamber maintenance.

- After dry etch, remove the PMMA by dipping the sample to acetone for 60 s and IPA for 60 s by repeated times (e.g., 3 times). Stirring the sample helps. Dry IPA with a gentle blow of nitrogen.
- Remove the remnant by descum using YES Plasma Stripper for 180 sec.
- Repeat cleaning with acetone (60 s) and IPA (60 s) and dry with gentle nitrogen blow.

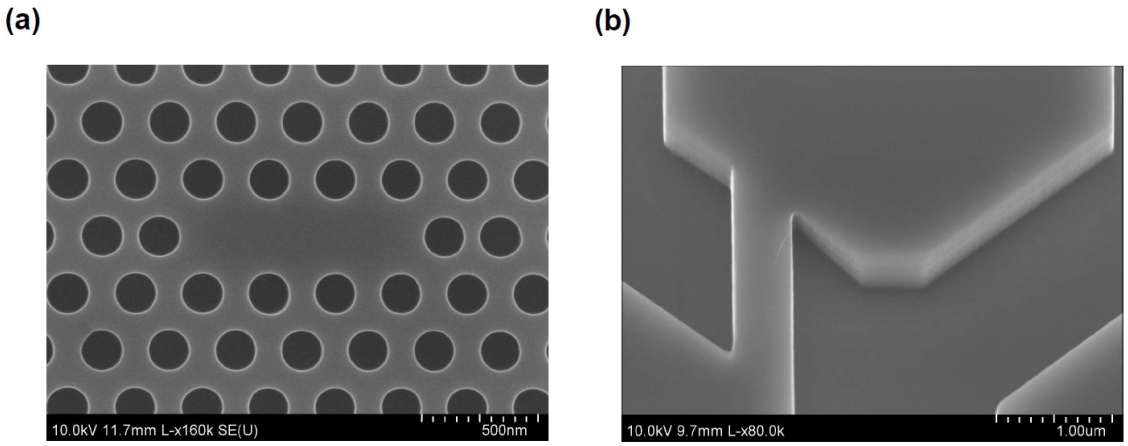

Figure A.3: Sample dry etched by Oxford PlasmaLab 100. (b) is a tilted image of an etched letter.

- Sometimes the sample can be under- or over-etched due to an inaccurate etch time.

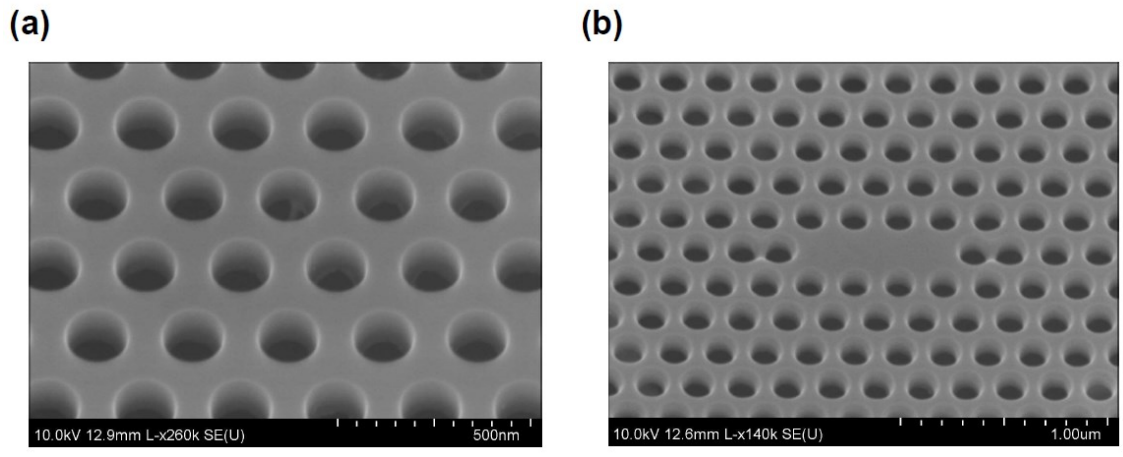

Figure A.4: SEM images of (a) underetched and (b) overetched samples after undercut.

A.4 Undercutting

- Prepare citric acid, 5 % hydrofluoric acid (HF), water, acetone and IPA in separate beakers.
- While performing the following steps, make sure that the sample surface is always covered by liquid and does not dry until using nitrogen.
- Dip the sample in citric acid for 60 s.
- Dip the sample in 5 % HF for 5 s and rinse in water for 25 s. Gently agitate the sample. Repeat this about 6 times. (Dipping the sample in HF for a longer time can damage the sample due to the hydrogen gas released during the etch.)
- Dip the sample in citric acid and rinse with acetone and IPA, each for 60 s.
- Dry the sample with gentle nitrogen blow.
- Check the sample by microscope. The color of the undercut area changes to pink due to the index contrast by an air gap as shown in Fig. A.5.

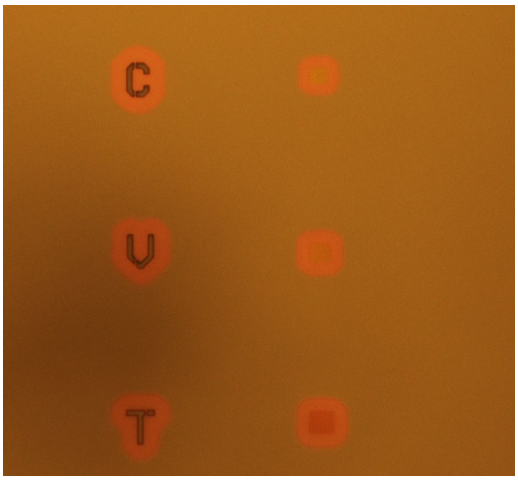

Figure A.5: Microscope image of sample after undercut.

- Image the sample by SEM and check if photonic crystals are suspended in air and free of debris [Fig. A.6].

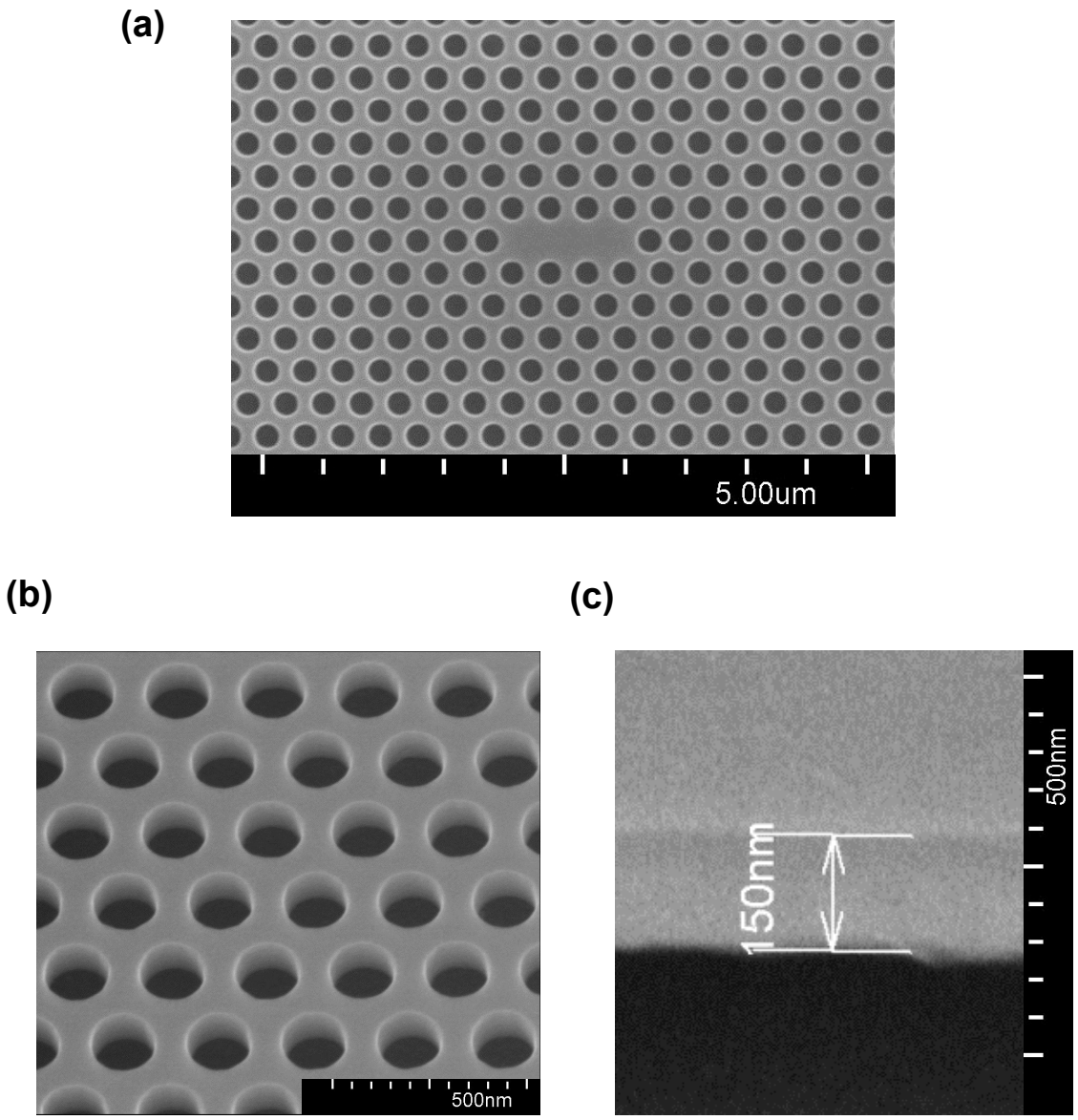

Figure A.6: SEM images of the final sample after undercut. Sample tilted by (a) 0°, (b) 30° and (c) 65°.

- If necessary, repeat the etching process, but adjust the number of dips into HF.

- Citric acid can additionally remove small debris on sample [Fig. A.7] by etching oxidized GaAs.

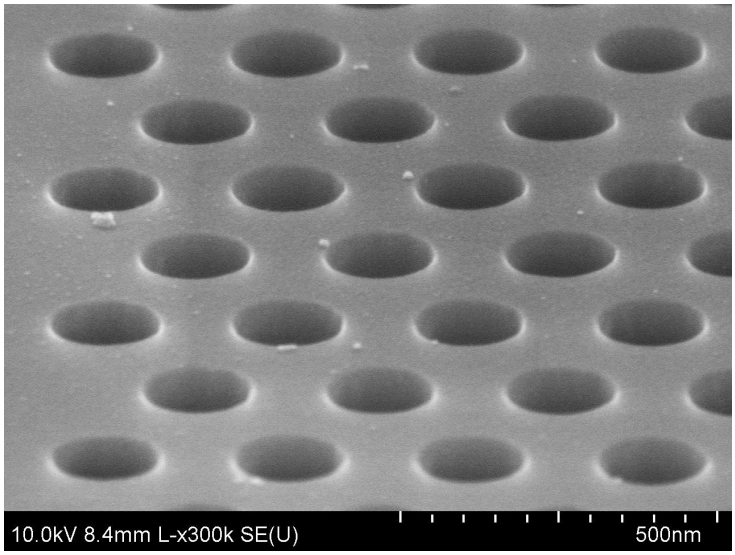

Figure A.7: Debris on sample before treated with citric acid.

Appendix B

Quantum Optical Toolbox

Quantum optical tool box is a matlab-based program that can simulate the time-evolution of a two-level system interacting with photons [97]. Here we look into the quantum optical background to understand the toolbox and follow the numerical solutions that lead to the simulation result in Chapter 6.

B.1 Jaynes-Cummings Hamiltonian

The Jaynes-Cummings Hamiltonian is a theoretical model that describes the coupling of an atomic two-level system to a quantized field of light. The two-level in a quantum dot, for example, consists of the combination of ground $|0\rangle$ and exciton $|X\rangle$ states. With this, we express the quantum objects such as states and operators using vectors and matrices in the simulation. In case of a two-level system ($|\psi\rangle = a|X\rangle + b|0\rangle$), we use the Pauli matrices to construct the ladder (transition) operators.

$$\sigma_x = \begin{pmatrix} 0 & 1 \\ 1 & 0 \end{pmatrix}, \qquad \sigma_y = \begin{pmatrix} 0 & -i \\ i & 0 \end{pmatrix}, \qquad \sigma_x = \begin{pmatrix} 1 & 0 \\ 0 & -1 \end{pmatrix} \tag{B.1}$$

The raising (lowering) operator that takes into account the transition from the ground (exciton) to exciton (ground) state can be written as the following.

$$\sigma_+ = \frac{1}{2}(\sigma_x + i\sigma_y) = \begin{pmatrix} 0 & 1 \\ 0 & 0 \end{pmatrix}, \qquad \sigma_- = \frac{1}{2}(\sigma_x - i\sigma_y) = \begin{pmatrix} 0 & 0 \\ 1 & 0 \end{pmatrix} \tag{B.2}$$

Using these we can define

$$\sigma_+\sigma_- = \begin{pmatrix} 1 & 0 \\ 0 & 0 \end{pmatrix} \tag{B.3}$$

and obtain the exciton state population by calculating $\langle \sigma_+\sigma_- \rangle$. Here the operators that describe the two-level system are 2×2 matrices.

The photon number (Fock) states, on the other hand, have dimension that corresponds to the number of photons. For example, if $N = 3$, the creation and annihilation operators are

$$a^+ = \begin{pmatrix} 0 & 0 & 0 \\ \sqrt{1} & 0 & 0 \\ 0 & \sqrt{2} & 0 \end{pmatrix} \qquad \text{and} \qquad a = \begin{pmatrix} 0 & \sqrt{1} & 0 \\ 0 & 0 & \sqrt{2} \\ 0 & 0 & 0 \end{pmatrix} \tag{B.4}$$

from the relation $\langle m|a|n\rangle = \sqrt{n}\delta_{m,n-1}$. Then the photon number operator is

$$a^+a = \begin{pmatrix} 0 & 0 & 0 \\ 0 & 1 & 0 \\ 0 & 0 & 2 \end{pmatrix}. \tag{B.5}$$

By calculating $\langle a^+a \rangle$, we can obtain the average photon number. Note that in the simulation we assume that the maximum photon number is small so that we can use a truncated Fock state basis.

Now, let us consider constructing the Hamiltonian operator for a two-level system interacting with a driving field, which is also called the Jaynes-Cummings Hamiltonian.

$$H = \omega_0 \sigma_+ \sigma_- + \omega_c a^+ a + ig(a^+ \sigma_- - a\sigma^+) + \mathcal{E}(e^{-i\omega_L t} a^+ + e^{i\omega_L t} a) \tag{B.6}$$

where ω_0 is the atomic transition frequency, ω_c is the cavity photon frequency and ω_L is the frequency of the classical driving field. g is the atom-photon interaction strength and $\mathcal{E}$ is the field amplitude. We have set $\hbar = 1$.

We can simplify the Hamiltonian by the rotating wave approximation. Moving to an interaction picture rotating at the driving field frequency,

$$H = (\omega_0 - \omega_L)\sigma_+ \sigma_- + (\omega_c - \omega_L) a^+ a + ig(a^+ \sigma_- - a\sigma^+) + \mathcal{E}(a^+ + a). \tag{B.7}$$

Note that $a^+\sigma_-$ $(a\sigma^+)$ is the tensor product which acts on the space of joint systems. From above, we next construct the equation of motion using the density matrix,

$$\frac{d\rho}{dt} = -i[H, \rho]. \tag{B.8}$$

However, a realistic system has dissipations as shown in Fig. 4.4. For example,the dissipation in the quantum dot decay can be incorporated in the equation as follows.

$$\left.\frac{d\rho}{dt}\right|_{XX} = -i[H, \rho]_{XX} - \gamma \rho_{XX} \tag{B.9}$$

$$\left.\frac{d\rho}{dt}\right|_{00} = -i[H, \rho]_{00} + \gamma \rho_{XX} \tag{B.10}$$

where γ is the exciton decay rate.

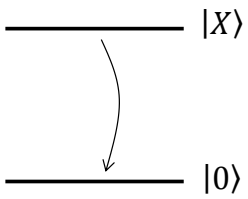

Figure B.1: Two-level system with a decay rate, γ.

We can involve the dissipations in the equation of motion by using the Liouvillian $\mathcal{L}$ which is a superoperator.

$$\mathcal{L}[D] = D\rho D^{+} - \frac{1}{2}D^{+}D\rho - \frac{1}{2}\rho D^{+}D \tag{B.11}$$

Including the cavity loss rate κ, two-level decay rate γ and pure dephasing rate γ_d, we arrive at the final equation of motion, which is also known as the master equation in Lindblad form.

$$\frac{d\rho}{dt} = -i[H,\rho] + 2\kappa\mathcal{L}[a] + 2\gamma\mathcal{L}[\sigma_{-}] + 2\gamma_d\mathcal{L}[\sigma_{+}\sigma_{-}] \tag{B.12}$$

By solving this equation, we can obtain $\rho(t)$ from which we calculate $\langle\sigma_{+}\sigma_{-}(t)\rangle$ and $\langle a^{+}a(t)\rangle$. Here the relation $\langle a\rangle = \mathrm{Tr}(a\rho)$ is used. Note that $\langle\sigma_{+}\sigma_{-}(t)\rangle$ is proportional to the spontaneous emission of a quantum dot.

B.2 Numerical Solution

The equation B.12 is solved by a numerical integration using the 'quantum optical toolbox'. In this section, we show a sample simulation result. The driving field is incorporated by a Gaussian pulse with a duration of 9 ps which is our estimation of the pulse width from the

laser autocorrelation.

Fig. B.2 shows the quantum dot spontaneous emission and cavity output as a function of time after excited by one pulse (a) and two time-delayed pulses (b). One can find that the cavity photon number increases initially by the pulse excitation which subsequently increase the quantum dot emission. Then the emitted photons from the dot are reabsorbed by the cavity which again increases the cavity photon number. Such coherent exchange happens because in the simulation the quantum dot, cavity, laser pulse are resonant with each other.

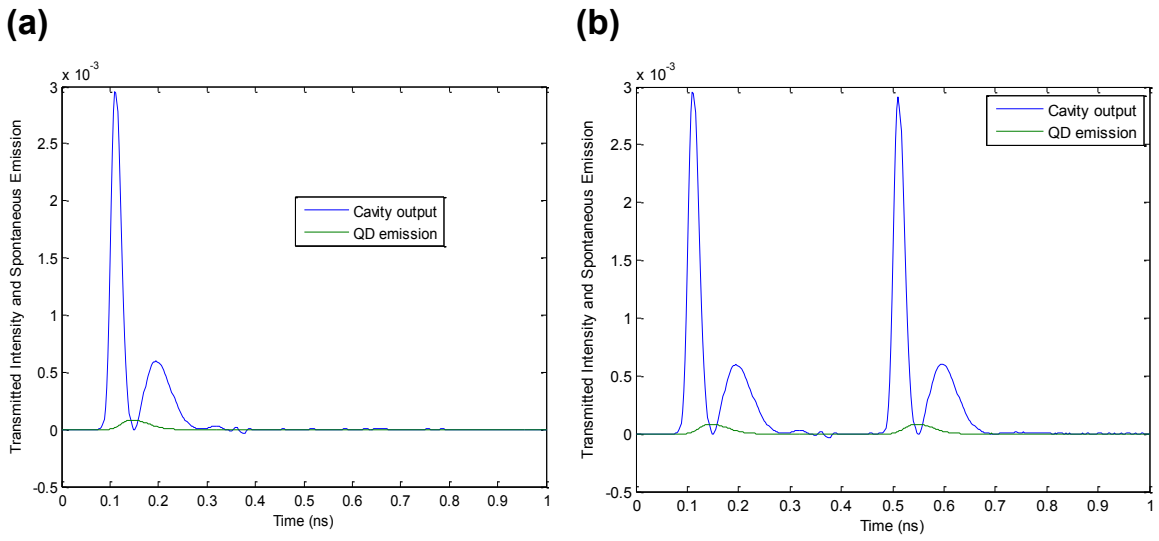

Figure B.2: QD excited state population and cavity photon number as a function of time, when excited by (a) single pulse and (b) time-delayed two pulses.

We then calculated the quantum dot spontaneous emission as a function of time with varying time-delay between two pulses in Fig. B.3 (a). As the time delay increases, the emission excited by the second pulse becomes more apparent. This is because the first pulse has saturated the quantum dot which hinder the excitation by the second pulse arriving before the dot decays. Since the exposure time of our detector (1 s) is much longer than the time

scale shown in the graph, we integrate the emissions with time and plot the total emission as a function of time-delay between the two pulses [Fig. B.3]. We can see that emission generally decreases near zero time-delay as a result of quantum dot saturation (nonlinearity). The slight bump at zero time delay may originate from the coherent interaction between the laser pulses, quantum dot and cavity.

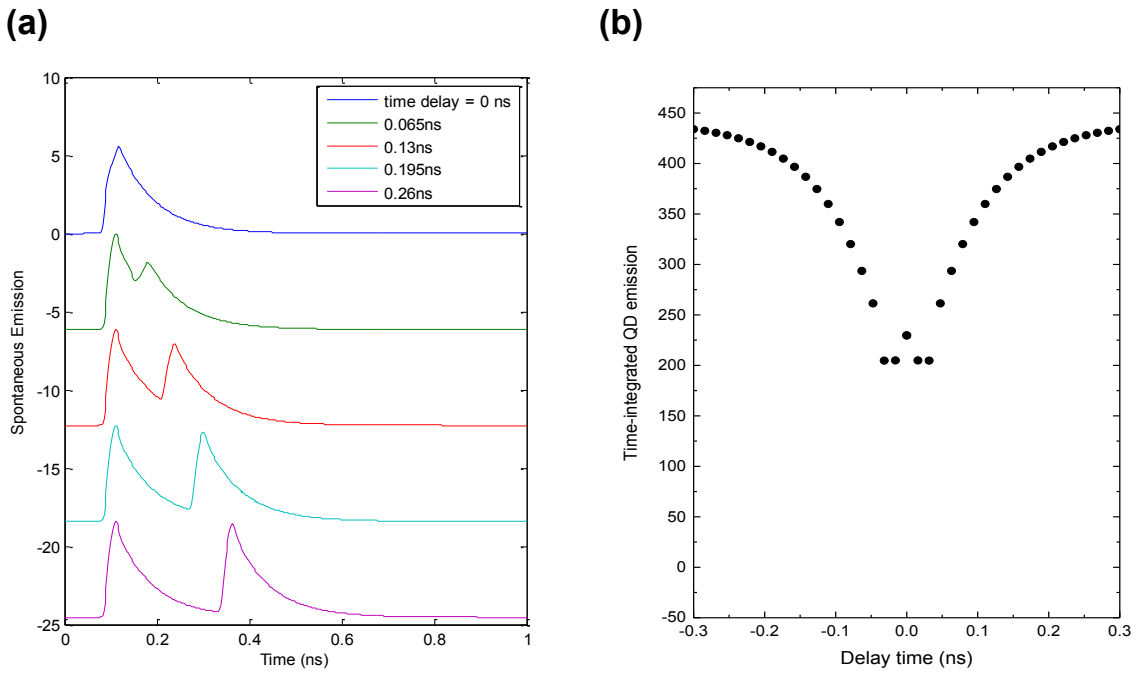

Figure B.3: QD spontaneous emission when excited by time-delayed two pulses. (a) Time evolution. (b) Time-integrated emission.

We also calculated the integrated quantum dot emission at a large time-delay for varying N in Fig. B.4. Although we have used truncated Fock states in the simulation, we obtained similar results for N $>$ 2. This indicates that the quantum dot saturation is intrinsically incorporated in the simulation and not originating from the limited photon numbers.

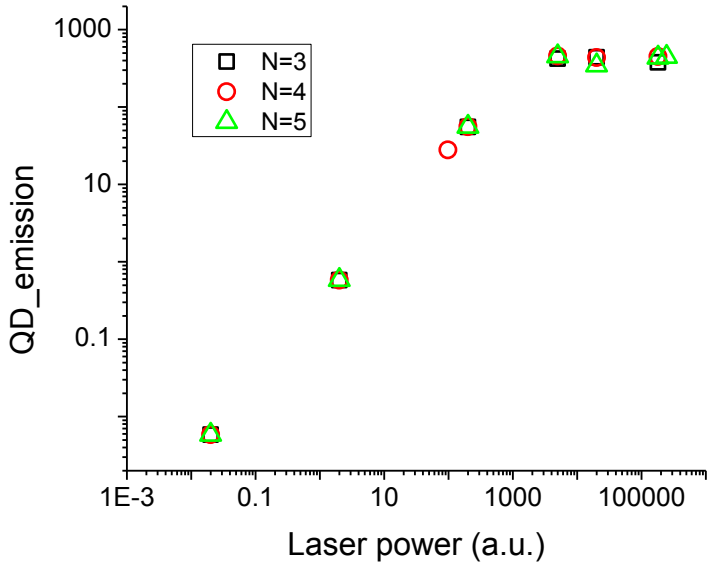

Figure B.4: Simulation as a function of laser power for selected photon numbers.

Bibliography

[1] Michler, P. (ed.) *Single Semiconductor Quantum Dots* (Springer, New York, NY, USA, 2009).

[2] DiVincenzo, D. P. Quantum Compuration. *Science* **270**, 255–261 (1995).

[3] Michler, P. *et al.* A quantum dot single-photon turnstile device. *Science* **290**, 2282 (2000). URL `http://www.ncbi.nlm.nih.gov/pubmed/11125136`.

[4] Santori, C., Pelton, M., Solomon, G., Dale, Y. & Yamamoto, Y. Triggered Single Photons from a Quantum Dot. *Phys. Rev. Lett.* **86**, 1502–1505 (2001). URL `http://link.aps.org/doi/10.1103/PhysRevLett.86.1502`.

[5] Atature, M. *et al.* Quantum-Dot Spin-State Preparation with Near-Unity Fidelity. *Science* **312**, 551–553 (2006).

[6] Li, X. *et al.* An all-optical quantum gate in a semiconductor quantum dot. *Science* **301**, 809–11 (2003). URL `http://www.ncbi.nlm.nih.gov/pubmed/12907794`.

[7] Englund, D. *et al.* Controlling the Spontaneous Emission Rate of Single Quantum Dots in a Two-Dimensional Photonic Crystal. *Phys. Rev. Lett.* **95**, 013904 (2005). URL `http://link.aps.org/doi/10.1103/PhysRevLett.95.013904`.

[8] Auffèves-Garnier, A., Simon, C., Gérard, J.-M. & Poizat, J.-P. Giant optical nonlinearity induced by a single two-level system interacting with a cavity in the Purcell regime. *Phys. Rev. A* **75**, 053823 (2007). URL `http://link.aps.org/doi/10.1103/PhysRevA.75.053823`.

[9] Englund, D. *et al.* Controlling cavity reflectivity with a single quantum dot. *Nature* **450**, 857 (2007). URL `http://www.ncbi.nlm.nih.gov/pubmed/18064008`.

[10] Englund, D. *et al.* Ultrafast Photon-Photon Interaction in a Strongly Coupled Quantum Dot-Cavity System. *Phys. Rev. Lett.* **108**, 093604 (2012). URL `http://link.aps.org/doi/10.1103/PhysRevLett.108.093604`.

[11] Loo, V. *et al.* Optical Nonlinearity for Few-Photon Pulses on a Quantum Dot-Pillar Cavity Device. *Phys. Rev. Lett.* **109**, 166806 (2012). URL `http://link.aps.org/doi/10.1103/PhysRevLett.109.166806`.

[12] Yoshie, T., Scherer, A. & Hendrickson, J. Vacuum Rabi splitting with a single quantum dot in a photonic crystal nanocavity. *Nature* **432**, 200 (2004). URL http://www.nature.com/nature/journal/v432/n7014/abs/nature03119.html.

[13] Hennessy, K. *et al.* Quantum nature of a strongly coupled single quantum dot-cavity system. *Nature* **445**, 896 (2007). URL http://www.ncbi.nlm.nih.gov/pubmed/17259971.

[14] Blattmann, R., Krenner, H. J., Kohler, S. & Hänggi, P. Entanglement creation in a quantum-dotnanocavity system by Fourier-synthesized acoustic pulses. *Phys. Rev. A* **89**, 012327 (2014). URL http://link.aps.org/doi/10.1103/PhysRevA.89.012327.

[15] Kiravittaya, S., Benyoucef, M., Zapf-Gottwick, R., Rastelli, a. & Schmidt, O. G. Ordered GaAs quantum dot arrays on GaAs(001): Single photon emission and fine structure splitting. *Appl. Phys. Lett.* **89**, 233102 (2006). URL http://scitation.aip.org/content/aip/journal/apl/89/23/10.1063/1.2399354.

[16] Pfau, T. J. *et al.* Site-controlled InAs quantum dots grown on a 55 nm thick GaAs buffer layer. *Appl. Phys. Lett.* **95**, 243106 (2009). URL http://scitation.aip.org/content/aip/journal/apl/95/24/10.1063/1.3265918.

[17] Schneider, C. *et al.* Lithographic alignment to site-controlled quantum dots for device integration. *Appl. Phys. Lett.* **92**, 183101 (2008). URL http://scitation.aip.org/content/aip/journal/apl/92/18/10.1063/1.2920189.

[18] Schneider, C. *et al.* Single site-controlled In(Ga)As/GaAs quantum dots: growth, properties and device integration. *Nanotechnology* **20**, 434012 (2009). URL http://www.ncbi.nlm.nih.gov/pubmed/19801767.

[19] Atkinson, P., Kiravittaya, S., Benyoucef, M., Rastelli, a. & Schmidt, O. G. Site-controlled growth and luminescence of InAs quantum dots using in situ Ga-assisted deoxidation of patterned substrates. *Appl. Phys. Lett.* **93**, 101908 (2008). URL http://scitation.aip.org/content/aip/journal/apl/93/10/10.1063/1.2980445.

[20] Albert, F. *et al.* Quantum efficiency and oscillator strength of site-controlled InAs quantum dots. *Appl. Phys. Lett.* **96**, 151102 (2010). URL http://scitation.aip.org/content/aip/journal/apl/96/15/10.1063/1.3393988.

[21] Mehta, M., Reuter, D., Melnikov, a., Wieck, a. D. & Remhof, a. Focused ion beam implantation induced site-selective growth of InAs quantum dots. *Appl. Phys. Lett.* **91**, 123108 (2007). URL http://scitation.aip.org/content/aip/journal/apl/91/12/10.1063/1.2786836.

[22] McKay, H., Rudzinski, P., Dehne, A. & Millunchick, J. M. Focused ion beam modification of surfaces for directed self-assembly of InAs/GaAs(001) quantum dots. *Nanotechnology* **18**, 455303 (2007). URL http://stacks.iop.org/0957-4484/18/i=45/a=455303?key=crossref.095402bfda4142beb8cfcef04498e0c3.

[23] Lee, J. Y., Noordhoek, M. J., Smereka, P., McKay, H. & Millunchick, J. M. Filling of hole arrays with InAs quantum dots. *Nanotechnology* **20**, 285305 (2009). URL http://www.ncbi.nlm.nih.gov/pubmed/19546494.

[24] Martín-Sánchez, J. *et al.* Single photon emission from site-controlled InAs quantum dots grown on GaAs(001) patterned substrates. *ACS Nano* **3**, 1513–7 (2009). URL http://www.ncbi.nlm.nih.gov/pubmed/19435304.

[25] Yakes, M. K. *et al.* Leveraging crystal anisotropy for deterministic growth of InAs quantum dots with narrow optical linewidths. *Nano Lett.* **13**, 4870–5 (2013). URL http://www.ncbi.nlm.nih.gov/pubmed/23987910.

[26] Caruge, J. M., Halpert, J. E., Wood, V., Bulović, V. & Bawendi, M. G. Colloidal quantum-dot light-emitting diodes with metal-oxide charge transport layers. *Nat. Photonics* **2**, 247–250 (2008). URL http://www.nature.com/doifinder/10.1038/nphoton.2008.34.

[27] Varangis, M. *et al.* Low-threshold quantum dot lasers with 201nm tuning range. *Electron. Lett.* **36**, 1544–1545 (2000).

[28] a.J Nozik. Quantum dot solar cells. *Phys. E Low-dimensional Syst. Nanostructures* **14**, 115–120 (2002). URL http://linkinghub.elsevier.com/retrieve/pii/S1386947702003740.

[29] Zhuang, L., Guo, L. & Chou, S. Y. Silicon single-electron quantum-dot transistor switch operating at room temperature. *Appl. Phys. Lett.* **72**, 1205 (1998). URL http://scitation.aip.org/content/aip/journal/apl/72/10/10.1063/1.121014.

[30] Imamoglu, A. *et al.* Quantum Information Processing Using Quantum Dot Spins and Cavity QED. *PRL* **83**, 4204 (1999).

[31] Singh, J. (ed.) *Electronic and Optoelectronic Properties of Semiconductor Structures* (Cambridge University Press, New York, NY, USA, 2007).

[32] Reithmaier, J. P. *et al.* Strong coupling in a single quantum dot-semiconductor microcavity system. *Nature* **432**, 197–200 (2004). URL http://www.ncbi.nlm.nih.gov/pubmed/15538362.

[33] Zrenner, a. *et al.* Coherent properties of a two-level system based on a quantum-dot photodiode. *Nature* **418**, 612 (2002). URL http://www.ncbi.nlm.nih.gov/pubmed/12167853.

[34] Bockelmann, U. Exciton relaxation. *PRB* **48**, 637–640 (1993).

[35] Empedocles, S., Norris, D. & Bawendi, M. Photoluminescence Spectroscopy of Single CdSe Nanocrystallite Quantum Dots. *Phys. Rev. Lett.* **77**, 3873–3876 (1996). URL http://www.ncbi.nlm.nih.gov/pubmed/10062330.

[36] Peterson, J. J. & Krauss, T. D. Fluorescence spectroscopy of single lead sulfide quantum dots. *Nano Lett.* **6**, 510 (2006). URL http://www.ncbi.nlm.nih.gov/pubmed/16522053.

[37] Matthiesen, C., Vamivakas, A. N. & Atatüre, M. Subnatural Linewidth Single Photons from a Quantum Dot. *Phys. Rev. Lett.* **108**, 093602 (2012). URL http://link.aps.org/doi/10.1103/PhysRevLett.108.093602.

[38] Berman, D., Zhitenev, N. B. & Ashoori, R. C. Observation of Quantum Fluctuations of Charge on a Quantum Dot. *PRL* **82**, 161–164 (1999).

[39] Krummheuer, B., Axt, V. & Kuhn, T. Theory of pure dephasing and the resulting absorption line shape in semiconductor quantum dots. *Phys. Rev. B* **65**, 195313 (2002). URL http://link.aps.org/doi/10.1103/PhysRevB.65.195313.

[40] Petta, J., Johnson, a., Marcus, C., Hanson, M. & Gossard, a. Manipulation of a Single Charge in a Double Quantum Dot. *Phys. Rev. Lett.* **93**, 186802 (2004). URL http://link.aps.org/doi/10.1103/PhysRevLett.93.186802.

[41] Baskaran, A. & Smereka, P. Mechanisms of Stranski-Krastanov growth. *J. Appl. Phys.* **111**, 044321 (2012). URL http://scitation.aip.org/content/aip/journal/jap/111/4/10.1063/1.3679068.

[42] Leonard, D., K, P. & M, P. P. Critical layer thickness for self-assembled InAs islands on GaAs. *Phys. Rev. B* **50**, 11687 (1994).

[43] Zhang, L. *et al.* Single photon emission from site-controlled InGaN/GaN quantum dots. *Appl. Phys. Lett.* **103**, 192114 (2013). URL http://scitation.aip.org/content/aip/journal/apl/103/19/10.1063/1.4830000.

[44] Martin, a. J., Saucer, T. W., Rodriguez, G. V., Sih, V. & Millunchick, J. M. Lateral patterning of multilayer InAs/GaAs(001) quantum dot structures by in vacuo focused ion beam. *Nanotechnology* **23**, 135401 (2012). URL http://www.ncbi.nlm.nih.gov/pubmed/22421025.

[45] Saucer, T. *et al.* Photoluminescence of patterned arrays of vertically stacked InAs/GaAs quantum dots. *Solid State Commun.* **151**, 269 (2011). URL http://linkinghub.elsevier.com/retrieve/pii/S0038109810007416.

[46] Luengo-Kovac, M., Saucer, T. W., Martin, A. J., Millunchick, J. & Sih, V. Analyzing pattern retention for multilayer focused ion beam induced quantum dot structures. *J. Vac. Sci. Technol. B Microelectron. Nanom. Struct.* **31**, 031208 (2013). URL http://scitation.aip.org/content/avs/journal/jvstb/31/3/10.1116/1.4804278.

[47] Schneider, C. *et al.* Single photon emission from a site-controlled quantum dot-micropillar cavity system. *Appl. Phys. Lett.* **94**, 111111 (2009). URL http://scitation.aip.org/content/aip/journal/apl/94/11/10.1063/1.3097016.

[48] Jöns, K. D. *et al.* Triggered indistinguishable single photons with narrow line widths from site-controlled quantum dots. *Nano Lett.* **13**, 126 (2013). URL http://www.ncbi.nlm.nih.gov/pubmed/23198958.

[49] Juska, G., Dimastrodonato, V., Mereni, L. O., Gocalinska, A. & Pelucchi, E. Towards quantum-dot arrays of entangled photon emitters. *Nat. Photonics* **7**, 527–531 (2013). URL http://dx.doi.org/10.1038/nphoton.2013.128.

[50] Gallo, P. *et al.* Integration of site-controlled pyramidal quantum dots and photonic crystal membrane cavities. *Appl. Phys. Lett.* **92**, 263101 (2008). URL http://scitation.aip.org/content/aip/journal/apl/92/26/10.1063/1.2952278.

[51] Dalacu, D. *et al.* Deterministic emitter-cavity coupling using a single-site controlled quantum dot. *Phys. Rev. B* **82**, 033301 (2010). URL http://link.aps.org/doi/10.1103/PhysRevB.82.033301.

[52] Lee, J. *et al.* Photoluminescence imaging of focused ion beam induced individual quantum dots. *Nano Lett.* **11**, 1040 (2011). URL http://pubs.acs.org/doi/abs/10.1021/nl1038902.

[53] Lee, J.-E. *et al.* Ground-state exciton emission of InAs quantum dots produced by focused-ion-beam-directed nucleation. *J. Lumin.* **133**, 117–120 (2013). URL http://linkinghub.elsevier.com/retrieve/pii/S0022231311005746.

[54] Suraprapapich, S., Thainoi, S., Kanjanachuchai, S. & Panyakeow, S. Self-assembled quantum-dot molecules by molecular-beam epitaxy. *J. Vac. Sci. Technol. B Microelectron. Nanom. Struct.* **23**, 1217 (2005). URL http://scitation.aip.org/content/avs/journal/jvstb/23/3/10.1116/1.1894417.

[55] Kiravittaya, S., Rastelli, A. & Schmidt, O. G. Advanced quantum dot configurations. *Reports Prog. Phys.* **72**, 046502 (2009). URL http://stacks.iop.org/0034-4885/72/i=4/a=046502?key=crossref.6d54e7379b000b8fc03e639cdf594aad.

[56] Wang, C. F. *et al.* Optical properties of single InAs quantum dots in close proximity to surfaces. *Appl. Phys. Lett.* **85**, 3423 (2004). URL http://scitation.aip.org/content/aip/journal/apl/85/16/10.1063/1.1806251.

[57] Bayer, M. & Forchel, a. Temperature dependence of the exciton homogeneous linewidth in In0.60Ga0.40As/GaAs self-assembled quantum dots. *Phys. Rev. B* **65**, 041308 (2002). URL http://link.aps.org/doi/10.1103/PhysRevB.65.041308.

[58] Pawley, J. (ed.) *Handbook of biological confocal microscopy* (Springer, Springer, NY, USA, 2006).

[59] Thon, S. M. *et al.* Strong coupling through optical positioning of a quantum dot in a photonic crystal cavity. *Appl. Phys. Lett.* **94**, 111115 (2009). URL http://scitation.aip.org/content/aip/journal/apl/94/11/10.1063/1.3103885.

[60] Xie, Q., Madhukar, A., Chen, P. & Kobayashi, N. Vertically Self-Organized InAs Quantum Box Islands on GaAs(100). *Phys. Rev. Lett.* **75**, 2542 (1995).

[61] Nakamura, Y. *et al. Jpn. J. Appl. Phys.* **43**, L362 (2004).

[62] Ho, K. M., Chan, C. T. & Soukoulis, S. M. Existence of a Photonic Gap in Periodic Dielectric Structures. *PRL* **65**, 3152 (1990).

[63] Joannopoulos, J. D., Villeneuve, P. R. & Fan, S. Photonic crystals: putting a new twist on light. *Nature* **386**, 143 (1997). URL `http://www.nature.com/nature/journal/v386/n6621/pdf/386143a0.pdf`.

[64] Walther, H., Varcoe, B. T. H., Englert, B.-G. & Becker, T. Cavity quantum electrodynamics. *Reports Prog. Phys.* **69**, 1325–1382 (2006). URL `http://stacks.iop.org/0034-4885/69/i=5/a=R02?key=crossref.2e5c0e61d04e1066e39543161ec7a7c4`.

[65] Purcell, E. M. *Phys. Rev. Lett.* **69**, 681 (1946).

[66] Scully, M. O. & Zubairy, M. S. (eds.) *Quantum Optics* (Cambridge University Press, New York, NY, USA, 1997).

[67] Khitrova, G. *et al.* Vacuum Rabi splitting in semiconductors. *Nat. Phys.* **2**, 81–90 (2006).

[68] Chang, W.-H. *et al.* Efficient Single-Photon Sources Based on Low-Density Quantum Dots in Photonic-Crystal Nanocavities. *Phys. Rev. Lett.* **96**, 117401 (2006). URL `http://link.aps.org/doi/10.1103/PhysRevLett.96.117401`.

[69] Schwagmann, A. *et al.* On-chip single photon emission from an integrated semiconductor quantum dot into a photonic crystal waveguide. *Appl. Phys. Lett.* **99**, 261108 (2011). URL `http://scitation.aip.org/content/aip/journal/apl/99/26/10.1063/1.3672214`.

[70] Fushman, I. *et al.* Controlled phase shifts with a single quantum dot. *Science* **320**, 769–72 (2008). URL `http://www.ncbi.nlm.nih.gov/pubmed/18467584`.

[71] Kim, H., Bose, R., Shen, T. C., Solomon, G. S. & Waks, E. A quantum logic gate between a solid-state quantum bit and a photon. *Nat. Photonics* **7**, 373 (2013).

[72] Rosfjord, K. M. *et al.* Nanowire single-photon detector with an integrated optical cavity and anti-reflection coating. *Opt. Express* **14**, 527–34 (2006). URL `http://www.ncbi.nlm.nih.gov/pubmed/19503367`.

[73] Joannopoulos, J. D. & Johnson, S. G. URL `http://ab-initio.mit.edu/wiki/index.php/Meep`.

[74] Joannopoulos, J. D., Johnson, S. G., Winn, J. N. & Meade, R. D. (eds.) *Photonic Crystals: Molding the Flow of Light* (Princeton University Press, Princeton, NJ, USA, 2008).

[75] Yee, K. Numerical Solution of Initial Boundary Value Problems Involving Maxwell's Equations in Isotropic Media. *IEEE Trans. Antennas Propag.* 302 (1966).

[76] Engquist, B. & Majdat, A. Absorbing boundary conditions. *PNAS* **74**, 1765–1766 (1977).

[77] Khankhoje, U. K. *et al.* Modelling and fabrication of GaAs photonic-crystal cavities for cavity. *Nanotechnology* **21**, 065202 (2010).

[78] Akahane, Y., Asano, T. & Song, B.-s. High- Q photonic nanocavity in a two-dimensional photonic crystal. *Nature* **425**, 944 (2003).

[79] Saucer, T. W. & Sih, V. Optimizing nanophotonic cavity designs with the gravitational search algorithm. *Opt. Express* **21**, 20831–20836 (2013).

[80] Chow, E. K., Lin, S.-Y., Johnson, S. G. & Joannopoulos, J. D. Transmission measurement of quality factor photonic crystal cavity. *Proceeding SPIE* **4646**, 199–204 (2002). URL `http://proceedings.spiedigitallibrary.org/proceeding.aspx?articleid=874584`.

[81] Gerardot, B. D., Subramanian, G., Minvielle, S., Lee, H. & Johnson, J. A. Self-assembling quantum dot lattices through nucleation site engineering. *J. Cryst. Growth* **236**, 647–654 (2002).

[82] Chalcraft, a. R. a. *et al.* Mode structure of the L3 photonic crystal cavity. *Appl. Phys. Lett.* **90**, 241117 (2007). URL `http://scitation.aip.org/content/aip/journal/apl/90/24/10.1063/1.2748310`.

[83] Asano, T., Song, B.-s., Akahane, Y. & Noda, S. Ultrahigh- Q Nanocavities in Two-Dimensional. *IEEE J. Sel. Top. Quantum Electron.* **12**, 1123 (2006).

[84] Tanabe, T., Notomi, M., Kuramochi, E., Shinya, A. & Taniyama, H. Trapping and delaying photons for one nanosecond in an ultrasmall high-Q photonic-crystal nanocavity. *Nat. Photonics* **1**, 49–52 (2007). URL `http://www.nature.com/doifinder/10.1038/nphoton.2006.51`.

[85] Lai, Y. *et al.* Genetically designed L3 photonic crystal nanocavities with measured quality factor exceeding one million. *Appl. Phys. Lett.* **104**, 241101 (2014). URL `http://scitation.aip.org/content/aip/journal/apl/104/24/10.1063/1.4882860`.

[86] Kiraz, A. *et al.* Cavity-quantum electrodynamics using a single InAs quantum dot in a microdisk structure. *Appl. Phys. Lett.* **78**, 3932 (2001). URL `http://link.aip.org/link/APPLAB/v78/i25/p3932/s1&Agg=doi`.

[87] Lodahl, P., Driel, A. F. V., Nikolaev, I. S. & Irman, A. Controlling the dynamics of spontaneous emission from quantum dots by photonic crystals. *Nature* **430**, 654 (2004).

[88] Strauf, S. *et al.* Self-Tuned Quantum Dot Gain in Photonic Crystal Lasers. *Phys. Rev. Lett.* **96**, 127404 (2006). URL `http://link.aps.org/doi/10.1103/PhysRevLett.96.127404`.

[89] Srinivasan, K. & Painter, O. Linear and nonlinear optical spectroscopy of a strongly coupled microdisk-quantum dot system. *Nature* **450**, 862–5 (2007). URL `http://www.ncbi.nlm.nih.gov/pubmed/18064009`.

[90] Bose, R., Sridharan, D., Kim, H., Solomon, G. & Waks, E. Low-Photon-Number Optical Switching with a Single Quantum Dot Coupled to a Photonic Crystal Cavity. *Phys. Rev. Lett.* **108**, 227402 (2012). URL `http://link.aps.org/doi/10.1103/PhysRevLett.108.227402`.

[91] Young, D., Zhang, L., Awschalom, D. & Hu, E. Coherent coupling dynamics in a quantum-dot microdisk laser. *Phys. Rev. B* **66**, 081307(R) (2002). URL `http://link.aps.org/doi/10.1103/PhysRevB.66.081307`.

[92] Laucht, A. *et al.* Temporal monitoring of nonresonant feeding of semiconductor nanocavity modes by quantum dot multiexciton transitions. *Phys. Rev. B* **81**, 241302(R) (2010). URL `http://link.aps.org/doi/10.1103/PhysRevB.81.241302`.

[93] Winger, M. *et al.* Explanation of Photon Correlations in the Far-Off-Resonance Optical Emission from a Quantum-DotCavity System. *Phys. Rev. Lett.* **103**, 207403 (2009). URL `http://link.aps.org/doi/10.1103/PhysRevLett.103.207403`.

[94] Lee, J., Saucer, T., Martin, A., Millunchick, J. & Sih, V. Time-Resolved Two-Pulse Excitation of Quantum Dots Coupled to a Photonic Crystal Cavity in the Purcell Regime. *Phys. Rev. Lett.* **110**, 013602 (2013). URL `http://link.aps.org/doi/10.1103/PhysRevLett.110.013602`.

[95] Su, L.-C., Wu, D.-C. & Mao, M.-H. Degenerate Pump Probe Photoluminescence Study on Quantum Dots Operating in Linear. *IEEE Photonics Technol. Lett.* **21**, 289 (2009).

[96] Bacher, G. *et al.* Biexciton versus Exciton Lifetime in a Single Semiconductor Quantum Dot. *Phys. Rev. Lett.* **83**, 4417–4420 (1999). URL `http://link.aps.org/doi/10.1103/PhysRevLett.83.4417`.

[97] Tan, S. M. A computational toolbox for quantum and atomic optics. *J. Opt. B Quantum Semiclassical Opt.* **1**, 424–432 (1999). URL `http://stacks.iop.org/1464-4266/1/i=4/a=312?key=crossref.5fdcf87f34c522f67efd471a0f2a1efe`.

[98] Kimble, H. J. Strong Interactions of Single Atoms and Photons in Cavity QED. *Phys. Scr.* **T76**, 127 (1998). URL http://www.physica.org/xml/article.asp?article=t076a00127.xml.

[99] Majumdar, A., Englund, D., Bajcsy, M. & Vučković, J. Nonlinear temporal dynamics of a strongly coupled quantum-dotcavity system. *Phys. Rev. A* **85**, 033802 (2012). URL http://link.aps.org/doi/10.1103/PhysRevA.85.033802.

[100] Hausmann, B. J. M., Bulu, I., Venkataraman, V., Deotare, P. & Lončar, M. Diamond nonlinear photonics. *Nat. Photonics* **8**, 369–374 (2014). URL http://www.nature.com/doifinder/10.1038/nphoton.2014.72.

[101] Yuan, Z. *et al.* Electrically driven single-photon source. *Science* **295**, 102 (2002). URL http://www.ncbi.nlm.nih.gov/pubmed/11743163.